ELSEVIER

High-pressure catalytic combustion of methane over platinum: In situ experiments and detailed numerical predictions

Michael Reinke, John Mantzaras,* Rolf Schaeren, Rolf Bombach, Andreas Inauen, and Sabine Schenker

Paul Scherrer Institute, Combustion Research, CH-5232 Villigen PSI, Switzerland

Abstract

The catalytic combustion of fuel-lean methane/air premixtures over platinum was investigated experimentally and numerically in the pressure range 4 to 16 bar. Experiments were performed in an optically accessible, laminar channel-flow catalytic reactor. In situ, spatially resolved Raman measurements of major species and temperature over the reactor boundary layer were used to assess the heterogeneous (catalytic) reactivity and planar laser-induced fluorescence (LIF) of the OH radical confirmed the absence of homogeneous (gas-phase) ignition. Numerical predictions were carried out with a two-dimensional elliptic code that included elementary heterogeneous and homogeneous chemical reaction schemes. Comparisons between measurements and numerical predictions have led to the assessment of the high-pressure validity of two different elementary heterogeneous chemical reaction schemes for the complete oxidation of methane over platinum. It was shown that the catalytic reactivity increased with increasing pressure and that crucial in the performance of the heterogeneous reaction schemes was the capture of the decrease in surface free-site availability with increasing pressure. Even in the absence of homogeneous ignition, the contribution of the gaseous reaction pathway to the conversion of methane could not be ignored at high pressures. The delineation of the regimes of significance for both heterogeneous and homogeneous pathways has exemplified the importance of the preignition gaseous chemistry in many practical high-pressure catalytic combustion systems. Sensitivity and reaction flux analyses were carried out on a validated elementary heterogeneous reaction scheme and led to the construction of reduced catalytic reaction schemes capable of reproducing accurately the catalytic methane conversion in the channel-flow configuration as well as in a surface perfectly stirred reactor (SPSR) and, when coupled to a homogeneous reaction scheme, the combined heterogeneous and homogeneous methane conversions. A global catalytic step could not reproduce the measured catalytic reactivity over the entire pressure range 4 to 16 bar.
© 2003 The Combustion Institute. Published by Elsevier Inc. All rights reserved.

Keywords: High-pressure methane catalytic combustion; In situ Raman measurements; Catalytic reactivity; Reduced heterogeneous reaction schemes

1. Introduction

The complete and partial catalytic oxidation of lower hydrocarbons over noble metals is of prime interest in many industrial applications ranging from power generation and microreactors to pollutant

* Corresponding author.
  E-mail address: ioannis.mantzaras@psi.ch
(J. Mantzaras).

Nomenclature

b	Channel half height, Fig. 1
B	Preexponential of global catalytic reaction, Eqs. (13) and (16)
c_p	Specific heat at constant pressure
Da_s	Surface Damköhler number, Eq. (20)
D_{km}	Mixture-average species diffusion coefficient, Eq. (7)
E_a	Effective activation energy, Eqs. (13) and (16)
F, G, H	Functions defined in Eqs. (21) and (23)
h, h_k^0	Total enthalpy, chemical enthalpy of the kth gaseous species
$I_{h,F}$	Fractional heterogeneous fuel conversion, Eq. (17)
k	Reaction rate coefficient, Eq. (11)
K_g	Total number of gaseous species, Eq. (5)
M_s	Total number of surface species, Eq. (6)
$\dot{m}_F(x)$	Local fuel mass flow rate per unit channel depth (z)
$\dot{m}_{h,F}(x)$	Integrated heterogeneous fuel conversion per unit depth (z)
L	Channel length, Fig. 1
Le	Lewis number of the fuel (thermal over species diffusivity)
m	Sum of surface reactants' stoichiometric coefficients, Eq. (11)
n	Pressure exponent of global catalytic reaction, Eqs. (13) and (16)
P	Function defined in Eq. (21)
p	Pressure
Pr	Prandtl number
R	Universal gas constant
SV	Surface-to-volume ratio, Eq. (14)
$\dot{s}_k$	Species heterogeneous molar production rates, Eq. (6)
T, T_0	Temperature, reference temperature in Eq. (8)
u, U_{IN}	Local streamwise velocity, inlet streamwise velocity
v	Transverse velocity

$\vec{V}_k$	Species diffusion velocity vector, Eq. (7)
$\dot{w}_k$	Gas-phase species molar production rate, Eq. (5)
W	Channel width, Fig. 1
$W_k, \overline{W}$	Gas-phase species molecular weight, average molecular weight
X_k	Gas-phase species mole fraction
Y_k	Gas-phase species mass fraction
$\tilde{Y}_F$	Normalized fuel mass fraction defined after Eq. (19)
x, y, z	Streamwise, transverse, and lateral physical coordinates, Fig. 1

Greek symbols

α_{th}	Thermal diffusivity, Eq. (20)
γ_k	Sticking coefficient, Eq. (11)
Γ	Surface site density, Eq. (11)
ζ	Nondimensional streamwise distance, Eq. (18)
$\theta_{T,k}$	Species thermal diffusion ratio, Eq. (7)
θ_m	Surface species coverage, Eq. (6)
λ	Thermal conductivity
μ	Viscosity
ρ	Density
σ_m	Surface species site occupancy, Eq. (6)
τ	Reactor residence time, Eq. (14)

Subscripts

ads	Adsorption, desorption
F	Fuel
h	Heterogeneous
IN	Inlet
k, m	Indices for gas-phase and surface species
W	Wall
x, y	Streamwise and transverse components

Superscripts

$'$	Differentiation with respect to the normalized transverse coordinate

abatement and chemical synthesis. In particular, the complete catalytic oxidation of natural gas has received increased attention in decentralized heat and power systems and in stationary gas turbines; the latter employ the catalytically stabilized combustion (CST) technology [1,2], whereby ultralow NO_x emissions can be achieved in a sequential heterogeneous (catalytic) and homogeneous (gas phase) hybrid combustion concept. The advancement of catalytic combustion in power systems requires the development

of catalysts with increased activity toward the complete oxidation of methane in fuel-lean air-fed combustion (methane is the main constituent of natural gas), the understanding of the heterogeneous and of the low-temperature homogeneous chemical kinetics of methane, and the availability of multidimensional numerical codes that can be used for reactor design. Moreover, the hetero/homogeneous kinetics and their interactions should be investigated under the high-pressure operating conditions of the aforemen-

tioned combustion systems. Validation of different elementary homogeneous reaction schemes in CST over platinum and investigation of the underlying hetero/homogeneous chemistry coupling were reported recently in Reinke et al. [3] for CH_4/air mixtures at pressures up to 10 bar and in Appel et al. [4] for H_2/air mixtures at atmospheric pressure; they assessed homogeneous ignition in a channel-flow catalytic reactor using planar laser-induced fluorescence (LIF) of the OH radical and—in conjunction with detailed numerical predictions—they clearly demonstrated substantial differences in the performance of various elementary gaseous reaction schemes.

Existing elementary heterogeneous chemical reaction schemes for the complete [5–7] and partial [6–9] oxidation of methane over platinum (the catalyst of interest in the present study) have relied primarily on ultra high vacuum (UHV) surface science data, notwithstanding recent advances of in situ surface science diagnostics [10]. The extension of the developed reaction schemes to realistic pressures and technical catalysts has necessitated appropriate kinetic rate modifications in order to bridge the well-known "pressure and materials gap." These modifications were aided by measurements of catalytic ignition, catalytic extinction, steady fuel conversion, and product selectivity in two basic reactor configurations: the nearly isothermal, low-temperature ($T \lesssim 600\,°C$), gradientless tubular or annular flow reactor [11,12] (fed with highly diluted fuel/oxidizer mixtures in order to maintain a minimal temperature rise) and the stagnation flow reactor [5,7,13,14]. Although the extraction of kinetic data is straightforward in the former configuration, the nearly isothermal operation poses inherent limitations in the description of processes that can be—for certain fuels—thermally controlled (for example, catalytic ignition). Stagnation flow configurations, on the other hand, have provided a wealth of data on catalytic ignition/extinction, steady fuel conversion and product selectivity under realistic temperatures and mixture compositions. The measurements, in conjunction with numerical predictions from well-established one-dimensional codes [13,14], have aided considerably the refinement of surface reaction mechanisms. Most experiments involved mainly measurements of global quantities (total fuel conversion, surface temperature, etc.) and were, therefore, better suited for the description of abrupt ignition/extinction transient phenomena rather than of steady processes where local experimental variations in the gas and/or on the surface could potentially affect the data interpretation.

In our recent atmospheric-pressure catalytic combustion studies of H_2/air over Pt [4], we introduced the methodology of in situ spatially resolved Raman measurements of gas-phase species concentrations in the boundary layer formed over a catalyst, as a direct way to assess the catalytic reactivity—as well as the gaseous reactivity when combined with OH LIF—under steady operating conditions. Other researchers have further adopted similar approaches: Sidwell et al. [15] studied the catalytic combustion of CH_4/air mixtures over Pd-substituted hexaluminates at atmospheric pressure with spatially resolved gas sampling over a stagnation-flow boundary layer. The validity of various heterogeneous reaction schemes for the total oxidation of methane at high pressures relevant to practical systems has not been addressed in the literature. In the present study we apply the aforesaid established methodology to investigate the catalytic combustion of CH_4/air over Pt at pressures up to 16 bar. Experiments were performed in an optically accessible catalytic channel-flow reactor, which was operated at sufficiently low temperatures that ensured kinetically controlled methane conversion away from the mass-transport limit. Fuel-lean CH_4/air premixtures ($\varphi = 0.35$ to 0.40) were investigated under laminar flow conditions, with surface temperatures and pressures in the ranges $780\ \text{K} \leqslant T \leqslant 1250\ \text{K}$ and $4\ \text{bar} \leqslant p \leqslant 16\ \text{bar}$, respectively. One-dimensional Raman measurements (across the channel transverse distance) provided the boundary layer profiles of major species and temperature, planar LIF of the OH radical along the streamwise plane of symmetry confirmed the absence of homogeneous ignition and the ensuing formation of a flame, and, finally, thermocouples embedded beneath the catalyst yielded the surface temperature distribution. Computations were carried out with an elliptic two-dimensional CFD code that included elementary heterogeneous and homogeneous chemical reaction schemes and detailed transport. Two recent heterogeneous reaction schemes for the total oxidation of methane over Pt [5,7] were investigated, with the main objectives of validating their applicability under high pressures and, subsequently, based on the validated elementary heterogeneous scheme(s), of developing reduced and—if possible—one-step surface reaction mechanisms. Particular objectives were to investigate the effect of pressure on catalytic reactivity, to elucidate the influence of gaseous chemistry during high-pressure catalytic combustion, and to address issues of high-pressure reactor performance in light of recent analytical studies that have identified the controlling parameters in channel-flow CST [16,17].

First the test rig, the Raman/LIF measuring techniques, and the numerical model are presented. The contribution of the homogeneous pathway to the conversion of methane at high pressures is then elaborated, followed by comparisons between measurements and numerical predictions that result in the assessment of the validity of the tested schemes. Sen-
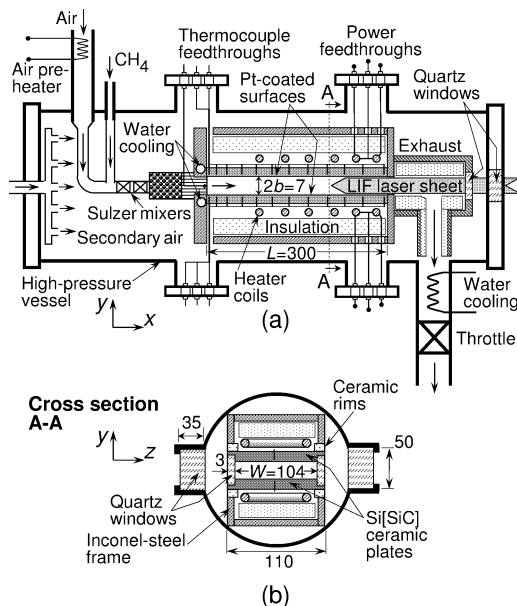
Fig. 1. Schematic of the catalytic reactor and the high-pressure vessel: (a) side view and (b) cross section. All distances are in mm. The enclosure $L \times W \times 2b$ defines the reactor volume.

sitivity and reaction flux analyses elucidate the differences among the heterogeneous schemes and lead to the development of reduced and global catalytic reaction mechanisms. Finally, the effect of pressure on catalytic reactor performance is addressed.

2. Experimental

2.1. Reactor configuration and test conditions

The test rig consisted of a channel-flow catalytic reactor, which formed a liner inside a high-pressure stainless-steel vessel (see Fig. 1). The reactor was similar to that used in earlier studies [3,4] and comprised two horizontal Si[SiC] ceramic plates, which were 300 mm long (L), 110 mm wide, 9 mm thick and placed 7 mm apart ($2b$). The ceramic plates were chamfered along their 300-mm sides in order to accommodate two 3-mm thick, 12-mm high, and 300-mm long quartz glass windows, which formed the reactor sidewalls. The lateral window separation was 104 mm (W) and the reactor volume was delineated by the $300 \times 104 \times 7\text{-mm}^3$ enclosure (see Fig. 1). In contrast to previous studies [4], the quartz windows were spring-pressed against the ceramic plates (with an intervening 1-mm-thick soft ceramic gasket) not on their center but on their four edges, thus allowing unobstructed optical access from both sides of the reactor. Four rectangular ceramic spacers, posi-

tioned at the chamfered corners of the Si[SiC] plates, maintained a constant 7-mm plate separation. Finally, the entire ceramic-plate and window assembly was mounted on an inconel-steel frame with the aid of ceramic support rims.

The catalyst surface temperature was monitored with 12 thermocouples on each plate (S type, 1 mm thick), positioned along the x–y plane of symmetry. The thermocouples were countersunk 0.9 mm beneath the catalytically active surfaces through 8.1-mm-deep and 1.2-mm in diameter holes eroded from the uncoated ceramic surfaces and were affixed inside their holes with alumina cement. In order to achieve the desired kinetically controlled fuel conversion and at the same time to sustain steady catalytic combustion at the relatively low laminar flow rates of this work, a combined cooling/heating arrangement was adopted: the $110 \times 9\text{-mm}^2$ entry sides of the ceramic plates were contacted to a water-cooled section of the inconel-steel frame, whereas the rear 200 mm of the plates was heated with two adjustable-power (up to 2.5 kW) resistive heating coils, which were positioned 15 mm above the thermocouples (see Fig. 1). A 50-mm-thick fiber ceramic insulation was placed on top of the heating coils to minimize the heat losses. With the above arrangement, the surface temperatures could be controlled to sufficiently low levels that not only allowed for finite-rate surface chemistry but also inhibited the onset of homogeneous ignition; the latter would have complicated the present catalytic reactivity studies. The combustion products were driven through an insulated cylindrical exhaust section to a water-cooled exit segment of the high-pressure tank. A 3-mm-thick and 50-mm in diameter quartz glass window positioned along the axis of the exhaust section provided an additional (streamwise) optical access.

An oil-free compressor provided dry air and high-pressure bottles supplied technical CH_4 (>99.5%). Both gases were regulated with two calibrated Brooks mass-flow controllers, having an accuracy better than 0.5%. The air was preheated by a 3-kW resistive heater and mixed with methane 25 cm upstream of the reactor (see Fig. 1a). A high degree of fuel/air premixedness was achieved with two sequential static Sulzer mixers (type SMV). After mixing, the flow was straightened in a 40-mm-long packing of 2-mm in diameter ceramic spheres and in a subsequent 40-mm-long inert ceramic honeycomb, leading to uniform velocity and temperature profiles at the reactor entry. An additional thermocouple, positioned inside one channel of the honeycomb, monitored the inlet temperature of the mixture.

The high-pressure vessel consisted of a 1.8-m-long and 0.28-m inside diameter cylindrical stainless-steel structure, rated to a maximum pressure of 60 bar.

The vessel was equipped with two high-pressure quartz glass windows (350 mm long, 35 mm thick, and 50 mm high, running parallel to the reactor side windows) that provided optical access from both sides of the reactor (see Fig. 1b). In addition, a counterflow streamwise optical access (used for the LIF experiments) was achieved through the reactor exhaust window and a 30-mm-thick and 30-mm in diameter high-pressure quartz glass window positioned at the center of the rear flange of the vessel (see Fig. 1a). The power supply and thermocouple lines were directed into the reactor via high-pressure feedthroughs on four dedicated tank flanges. The tank pressure was measured with a Fuji-Electric pressure transmitter and was regulated through a PID-controlled pneumatic exhaust gas throttle. During the experiments, a continuous flow of secondary air through a distribution ring cooled the tank walls and flushed the volume between the reactor and the high-pressure tank from any undesirable combustion products.

The laminar experimental conditions are given in Table 1 and span the pressure range 4 bar $\leqslant p \leqslant$ 16 bar. At $p < 4$ bar the recorded methane Raman signal was too weak; the same methane signal-to-noise considerations dictated the minimum fuel-to-air equivalence ratio ($\varphi = 0.35$). Safety considerations determined the higher equivalence ratio ($\varphi = 0.40$): larger φ resulted in high surface temperatures that endangered long-term catalyst stability. The Reynolds numbers of Table 1 were based on the uniform inlet properties and the channel hydraulic diameter ($= 13.1$ mm) and were kept below 2000, even though the strong flow laminarization induced by the heat transfer from the hot catalytic plates guaranteed laminar flow conditions at considerably higher incoming Reynolds numbers [18]. Case 16 was the only one of Table 1 with homogeneous ignition and flame formation and was included to facilitate the ensuing discussion on catalytic reactivity.

2.2. Catalyst preparation

The inner surfaces of the Si[SiC] plates were coated with Pt using plasma vapor deposition (PVD): a 1.5-μm-thick nonporous Al_2O_3 layer was first deposited on the ceramic surface, followed by a 2.2-μm-thick Pt layer. The very thick Pt coating on a nonporous structure closely resembled a polycrystalline Pt surface, and this was verified with independent surface area and surface composition measurements. The surface area was measured with BET in ceramic wafers 1 mm thick and 75 mm in diameter, coated with exactly the same PVD procedure as the catalytic plates of the reactor; fresh samples and samples exposed to the combustion environment of this study were analyzed. The total and active surface areas were
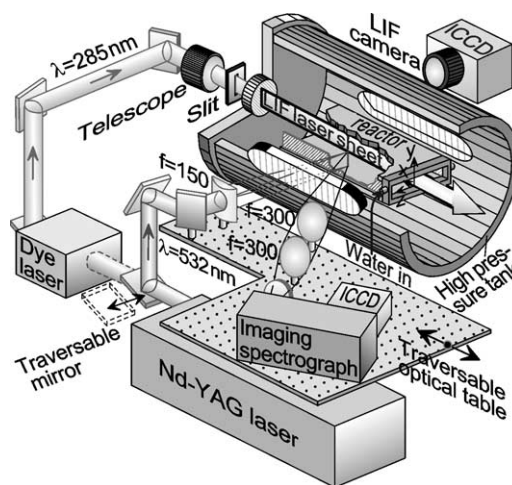
Fig. 2. Schematic of the OH planar laser-induced fluorescence (LIF) and Raman setup. All focal lengths are in mm.

measured with Kr physisorption and CO chemisorption, respectively. Tests with krypton were necessary as the nonporous nature of the catalyst resulted in a very small surface area (practically equal to the geometrical area) not measurable with standard N_2 physisorption. The BET measurements confirmed the absence of porous surface structure and, moreover, showed that the total and active surface areas were the same, indicating a surface covered completely with Pt. The latter was also verified with independent X-ray photoelectron spectroscopy (XPS) surface composition analyses of the reactor catalytic plates before and after the combustion experiments; the XPS analyses have shown that the surface was covered with Pt and that Al or Si did not diffuse on the surface even after extended reactor operation. A Pt surface site density of 2.7×10^{-9} mol/cm^2 (the value of polycrystalline Pt [5]) was, therefore, used in the numerical analysis.

2.3. Laser diagnostics

The Raman and planar LIF setup is depicted in Fig. 2. In the Raman experiment, a frequency-doubled Nd:YAG pulsed laser (Quantel YG781C20, 20-Hz repetition rate) provided the excitation source. The pulse energy and duration of the 532-nm radiation was 180 mJ and 14 ns, respectively. The laser beam was first expanded to a diameter of 2 cm by a spherical lens telescope and then focused through the tank and reactor side windows into a vertical line inside the reactor (~0.3 mm thick) by an $f = 150$-mm cylindrical lens. The focal line spanned the entire 7-mm transverse channel separation and was 15 mm offset from the x–y symmetry plane ($z = 15$ mm) to increase the collection angle and minimize thermal beam steering.

Table 1
Experimental conditions[a]

Case	p (bar)	φ	U_{IN} (m/s)	T_{IN} (K)	Re_{IN}
1	4	0.40	2.05	624	1926
2	4	0.35	2.02	633	1854
3	6	0.40	0.51	587	796
4	6	0.36	0.51	590	790
5	7	0.40	1.16	624	1907
6	7	0.35	1.15	627	1870
7	8	0.36	0.38	587	800
8	10	0.40	0.81	621	1915
9	10	0.35	0.80	627	1869
10	12	0.40	0.66	612	1936
11	12	0.35	0.68	627	1910
12	14	0.40	0.55	604	1921
13	14	0.35	0.55	606	1908
14	16	0.35	0.45	586	1898
15	16	0.35	0.46	592	1887
16	16	0.36	0.44	636	1616

[a] Pressure, equivalence ratio, inlet velocity, temperature, and Reynolds number.

Given the large cross-flow aspect ratio of the reactor ($\sim$15:1), the combustion processes were two dimensional with no lateral dependence (apart from zones extending up to 15 mm from each window, as also discussed in previous works [4]). Therefore, the lateral offset of the Raman measurements did not impact the forthcoming comparisons with 2-D numerical predictions. Two 76-mm-diameter lenses ($f = 300$ mm) collected the scattered light, at a 50° angle with respect to the sending optical path, and focused it to the entrance slit of a 25-cm imaging spectrograph (Chromex 250i). The dispersed light was recorded on an intensified CCD camera (LaVision Flame-Star 2F, 576 × 384 pixels). The 576- and 384-pixel-long CCD dimensions corresponded to wavelength and transverse distance, respectively; in the latter dimension, only 250 pixels spanned the 7-mm channel gap. A holographic notch filter (Kaiser Optical Systems, HNPF) and an OG-550 colored glass filter were placed before the spectrograph slit to attenuate the intense Rayleigh signal and the stray laser light scattered from the mechanical components of the test rig. As the flow conditions were steady and laminar, an average of 2000 images was used to improve the signal-to-noise ratio. The spectral dispersion on the CCD camera ranged from 1250 to 5000 cm^{-1}, allowing observation of all major species (O_2, N_2, CH_4, H_2O, and CO_2); the Raman shift ranged from 1388 cm^{-1} (CO_2) to 3652 cm^{-1} (H_2O). To further increase the signal-to-noise ratio, the spectrograph slit was opened to 0.4 mm; an almost top-hat slit transfer function with a width of about 60 to 80 cm^{-1} (depending on spectral position) was thus attained that still allowed for ample spectral separation of the Raman-shifted species lines and the background stray

light on the CCD array. The signal-to-noise considerations should not be understated in 1-D Raman combustion measurements of hydrocarbons, which require visible light excitation sources to minimize fluorescence interferences. In contrast to our previous atmospheric-pressure H_2/air CST studies [4] where a UV excimer laser source provided a much stronger Raman signal (owing to its ω^4 dependence, with ω the laser light frequency), the present work relied heavily on the effect of pressure to achieve sufficient signals: pressures below 4 bar were not amenable for 1-D Raman measurements of lean ($\varphi \leqslant 0.4$) CH_4/air mixtures.

The Raman data were referenced to a room temperature distribution of nitrogen inside the combustion channel. The effective Raman cross sections, which included transmission efficiencies (i.e., windows, lenses, filter, spectrometer, and camera), were evaluated by recording the signals of pure CH_4, air, and completely burnt exhaust gases of known composition. The background signal was fitted to a polynomial curve to account for the spectral variation of the stray light. An initial guess of the temperature distribution inside the channel was derived from the nitrogen signal assuming ideal gas behavior. This distribution was further used to correct all temperature-dependent Raman cross sections. For the diatomic species, theoretical harmonic oscillator Raman cross-section variations have been used [19]; for CH_4 and H_2O the data from Steiner [20] and Eisenberg [21], respectively, were employed. The corrected Raman cross sections provided an updated temperature distribution; a converged temperature distribution was achieved by repeating the entire process for a few times. The Raman signal of methane, which was the

deficient reactant, was of prime interest for the determination of the catalytic reactivity. In addition to CH_4, the H_2O and O_2 Raman lines were evaluated; the CO_2 line suffered from low signal-to-noise ratio given its low concentration (the lowest of all major species), its moderate Raman cross section (the lowest of all species having more than two atoms), and its unfavorable spectral position within a region of considerable background radiation. Raman measurements were acquired at streamwise intervals of 10 mm (and in some cases 20 mm) by traversing axially an optical table that supported the sending and collecting optics, including the spectrograph (see Fig. 2). The optical arrangement limited the streamwise extent of the Raman measurements to 15.5 mm $\leqslant x \leqslant$ 163.5 mm. The 250-pixel-long transverse distance was binned to 63 pixels, providing a y resolution of 0.11 mm. Raman data points closer than 0.6 mm to both catalyst surfaces were discarded due to low signal-to-noise ratio.

For the OH-LIF tests, the second harmonic of the Nd:YAG laser pumped a tunable dye laser (Quantel TDL50) with a frequency-doubled radiation at 285.09 nm and a pulse duration of 10 ns. A traversable mirror directed the 532-nm radiation either toward the Raman setup or toward the dye laser and the LIF setup (Fig. 2). As the experimental conditions where steady and laminar, simultaneous acquisition of Raman and OH-LIF data was not necessary; the LIF was recorded at regular intervals in-between the Raman data acquisition. The OH-LIF tests assured that there was no homogeneous ignition and flame formation, events that were increasingly likely at elevated pressures [3]. The laser beam was transformed into a vertical laser sheet by a cylindrical/spherical lens telescope and entered the reactor in a counterflow direction through the tank and reactor-exhaust quartz windows (see Figs. 1a and 2). The fluorescence of both OH (1–1) and (0–0) transitions at 308 and 314 nm, respectively, was collected at 90° through the second set of tank and reactor side windows with another CCD camera, identical to that of the Raman setup. Details of the OH setup have been provided elsewhere [3,4, 22].

3. Numerical model

3.1. Governing equations and boundary conditions

An elliptic, two-dimensional, steady model was used and numerical solution was obtained for the following governing equations.

Continuity equation:

$$\frac{\partial(\rho u)}{\partial x} + \frac{\partial(\rho v)}{\partial y} = 0. \tag{1}$$

Momentum equations:

$$\frac{\partial(\rho u u)}{\partial x} + \frac{\partial(\rho v u)}{\partial y} + \frac{\partial p}{\partial x}$$
$$- \frac{\partial}{\partial x}\left[2\mu\frac{\partial u}{\partial x} - \frac{2}{3}\mu\left(\frac{\partial u}{\partial x} + \frac{\partial v}{\partial y}\right)\right]$$
$$- \frac{\partial}{\partial y}\left[\mu\left(\frac{\partial u}{\partial y} + \frac{\partial v}{\partial x}\right)\right] = 0, \tag{2}$$

$$\frac{\partial(\rho u v)}{\partial x} + \frac{\partial(\rho v v)}{\partial y} + \frac{\partial p}{\partial y} - \frac{\partial}{\partial x}\left[\mu\left(\frac{\partial v}{\partial x} + \frac{\partial u}{\partial y}\right)\right]$$
$$- \frac{\partial}{\partial y}\left[2\mu\frac{\partial v}{\partial y} - \frac{2}{3}\mu\left(\frac{\partial u}{\partial x} + \frac{\partial v}{\partial y}\right)\right] = 0. \tag{3}$$

Energy equation:

$$\frac{\partial(\rho u h)}{\partial x} + \frac{\partial(\rho v h)}{\partial y} + \frac{\partial}{\partial x}\left(\rho \sum_{k=1}^{Kg} Y_k h_k V_{k,x} - \lambda\frac{\partial T}{\partial x}\right)$$
$$+ \frac{\partial}{\partial y}\left(\rho \sum_{k=1}^{Kg} Y_k h_k V_{k,y} - \lambda\frac{\partial T}{\partial y}\right) = 0. \tag{4}$$

Gas-phase species equations:

$$\frac{\partial(\rho u Y_k)}{\partial x} + \frac{\partial(\rho v Y_k)}{\partial y} + \frac{\partial}{\partial x}(\rho Y_k V_{k,x})$$
$$+ \frac{\partial}{\partial y}(\rho Y_k V_{k,y}) - \dot{w}_k W_k = 0,$$
$$k = 1, 2, \ldots, K_g. \tag{5}$$

Surface species coverage equations:

$$\frac{\partial \theta_m}{\partial t} = \sigma_m\frac{\dot{s}_m}{\Gamma} - \frac{\theta_m}{\Gamma}\dot{\Gamma}, \quad m = 1, 2, \ldots, M_s. \tag{6}$$

It is understood that only the steady-state solutions of Eqs. (6) are of interest in the present study and that gravity is not important for the high Reynolds numbers of Table 1.

The species diffusion velocities $\vec{V}_k$ were determined using the mixture average diffusion plus thermal diffusion for the light species [23]:

$$\vec{V}_k = -[D_{km}/X_k]\nabla X_k$$
$$+ \left[D_{km}\theta_{T,k}/(X_k T)\right]\nabla T. \tag{7}$$

Finally, the ideal gas and caloric equations of state were

$$p = \rho R T/\bar{W} \quad \text{and} \quad h_k = h_k^0(T_0) + \int_{T_0}^{T} c_{p,k}\, dT, \tag{8}$$

respectively. The boundary conditions at the gas-wall interfaces ($y = 0$ and $y = 2b$), were

$$(\rho Y_k V_{k,y})_{y=0} = W_k(\dot{s}_k)_{y=0},$$
$$(\rho Y_k V_{k,y})_{y=2b} = W_k(\dot{s}_k)_{y=2b} \tag{9}$$

and

$$T(x, y = 0) = T_{W,L}(x),$$

$$T(x, y = 2b) = T_{W,U}(x). \tag{10}$$

$T_{W,L}(x)$ and $T_{W,U}(x)$ were the thermocouple-measured temperature distributions of the lower and upper walls, respectively. Equations (10) were an improvement to previous homogeneous ignition CST works [3,4] that used the average (between upper and lower walls) temperature profile as a boundary condition for simulations over half the channel domain ($0 \leqslant y \leqslant b$). The earlier approach was adequate in the aforesaid homogeneous ignition studies, which were characterized by high surface temperatures with random upper/lower wall surface temperature differences—at any given axial position—of ± 8 K. In the present study, however, the lower operating temperatures and the absence of a flame in the reactor resulted in systematic temperature plate differences as large as 60 K, necessitating computations over the entire channel domain ($0 \leqslant y \leqslant 2b$). No-slip boundary conditions were applied at the walls for both velocity components. The inlet conditions were uniform profiles for the temperature T_{IN} (measured), the axial velocity U_{IN} (deduced from the inlet temperature and the measured mass-flow rates), and the species mass fractions. Finally, $v = 0$ and zero-Neumann conditions for all other scalars were applied at the end of the computational domain, which was taken at $x = 180$ mm.

The governing equations were discretized using a finite volume approach and solution was obtained iteratively with a SIMPLER [24] method for the pressure-velocity field; details on the solution algorithm have been provided elsewhere [4,25]. An orthogonal staggered grid of 350×120 points (in x and y, respectively) with finer x spacing toward the entrance and y spacing toward the wall was sufficient to produce a grid-independent solution. In addition to the elliptic model, a simpler and computationally faster parabolic (boundary layer) model was also used (details are given in Ref. [26]), with elementary hetero/homogeneous chemical reaction schemes and detailed transport; solution of the discretized algebraic-differential set of equations was obtained via marching in x. In the absence of homogeneous ignition, which could invalidate the boundary-layer approximation by inducing significant axial gas-phase gradients [26], both elliptic and parabolic models yielded exactly the same result. This was not surprising, as the parabolic model has been shown [27] to be valid in purely heterogeneous combustion at Reynolds numbers as low as 20, a value considerably lower than the Reynolds numbers of Table 1.

3.2. Chemical kinetics

Two elementary heterogeneous reaction schemes for the total oxidation of CH_4 on Pt were investigated (see Table 2), further denoted as Deutschmann et al. [5] and Vlachos and co-workers [7]. It is worth pointing that the scheme of Vlachos has been developed for both complete and partial catalytic oxidation applications. The adsorption reactions were calculated as

$$k_{\text{ads},k} = C \frac{\gamma_k}{\Gamma^m} \sqrt{\frac{RT}{2\pi W_k}}, \tag{11}$$

with C the Motz correction factor, $C = (1 - \theta_{\text{Pt}}\gamma_k/2)^{-1}$, as proposed in [25]. In Vlachos' scheme no correction was implemented and $C = 1$ [28]; nevertheless, the inclusion of the correction factor had a negligible impact on the performance of this scheme under the conditions of Table 1. In Deutschmann's heterogeneous scheme, the reverse rates of reactions 15–17 (see Table 2) were calculated using the forward rate coefficients and surface thermochemical data [29]. The surface site density was $\Gamma = 2.7 \times 10^{-9}$ mol/cm^2 as discussed in Section 2. Although the OH-LIF experiments assured no homogeneous ignition for Cases 1–15, the preignition gaseous chemistry could not be ignored at high pressures, as will be further elaborated in the following section. In our previous [3] high-pressure homogeneous ignition studies of CH_4/air over Pt (conducted under mass-transport-limited catalytic operation), the elementary gas-phase scheme of Warnatz and Maas [30] was validated over the pressure range 1 bar $\leqslant p \leqslant$ 6 bar; however, at 8 bar $\leqslant p \leqslant$ 10 bar, the scheme overpredicted the measured homogeneous ignition distances. On the other hand, the gas-phase scheme of GRI-3.0 [31] was shown [3] to be unrealistically fast, as it underpredicted substantially the measured homogeneous ignition distances at all pressures (1 bar $\leqslant p \leqslant$ 10 bar). Ongoing homogeneous ignition studies of our group at pressures of up to 16 bar have shown that the more recent scheme of Warnatz et al. [32] (further denoted as Warnatz) provided very good homogeneous ignition predictions in the range 6 bar $\leqslant p \leqslant$ 16 bar, and progressively earlier predictions as the pressure was reduced from 6 to 1 bar. To maintain the present catalytic reactivity studies free from homogeneous pathway contributions, the analysis considered only the initial reactor extent over which the gas-phase participation was negligible. The delineation of this extent required computations with either an accurate or at least a conservative gaseous scheme (i.e., a scheme that predicted an earlier homogeneous ignition). We have, therefore, opted to use two schemes: Warnatz [32], which was accurate over the high-pressure range 6 bar $\leqslant p \leqslant$ 16 bar and somewhat

Table 2
Heterogeneous chemical reaction mechanisms[a]

		Deutschmann[b]		Vlachos[c]			
		$A\,(\gamma)$	E	$A_f\,(\gamma)$	E_f	A_b	E_b
Adsorption reactions							
1.	$CH_4 + 2Pt(s) \rightarrow CH_3(s) + H(s)$	0.01	0.0	1.0	50.2	–	
2.	$O_2 + 2Pt(s) \rightarrow 2O(s)$	0.023	0.0	0.03	0.0	–	
3.	$O_2 + 2Pt(s) \rightarrow 2O(s)$	4.9×10^{12}	0.0	–	–	–	–
4.	$CH_3 + Pt(s) \rightarrow CH_3(s)$	–	–	1.0	0.0	–	–
5.	$CH_2 + Pt(s) \rightarrow CH_2(s)s$	–	–	1.0	0.0	–	–
6.	$CH + Pt(s) \rightarrow CH(s)$	–	–	1.0	0.0	–	–
7.	$C + Pt(s) \rightarrow C(s)$	–	–	1.0	0.0	–	–
8.	$H_2 + 2Pt(s) \rightarrow 2H(s)$	0.046	0.0	0.25	0.0	–	–
9.	$H + Pt(s) \rightarrow H(s)$	1.0	0.0	1.0	0.0	–	–
10.	$O + Pt(s) \rightarrow O(s)$	1.0	0.0	1.0	0.0	–	–
11.	$H_2O + Pt(s) \rightarrow H_2O(s)$	0.75	0.0	0.7	0.0	–	–
12.	$OH + Pt(s) \rightarrow OH(s)$	1.0	0.0	1.0	0.0	–	–
13.	$CO_2 + Pt(s) \rightarrow CO_2(s)$	–	–	1.0	0.0	–	–
14.	$CO + Pt(s) \rightarrow CO(s)$	0.84	0.0	1.0	0.0	–	–
Pure surface reactions							
15.	$H(s) + O(s) = OH(s) + Pt(s)$	1.0×10^{13}	11.5	1.7×10^{10}	50.6	5.6×10^{11}	102.1
16.	$H(s) + OH(s) = H_2O(s) + Pt(s)$	1.0×10^{13}	17.4	3.5×10^{11}	51.9	1.2×10^{10}	77.0
17.	$OH(s) + OH(s) = H_2O(s) + O(s)$	1.0×10^{13}	48.2	1.0×10^{11}	79.1	1.0×10^{11}	52.7
18.	$C(s) + OH(s) \rightarrow CO(s) + H(s)$	–	–	1.0×10^{11}	16.7	1.0×10^{11}	168.6
19.	$C(s) + O(s) \rightarrow CO(s) + Pt(s)$	1.0×10^{13}	62.8	1.0×10^{11}	18.0	–	–
20.	$CO(s) + Pt(s) \rightarrow C(s) + O(s)$	2.7×10^9	184.0	1.0×10^{11}	221.8	–	–
21.	$CO(s) + O(s) \rightarrow CO_2(s) + Pt(s)$	1.0×10^{13}	105.0	1.0×10^{11}	15.1	1.0×10^{11}	88.7
22.	$CO(s) + OH(s) \rightarrow CO_2(s) + H(s)$	–	–	1.0×10^{11}	35.1	1.0×10^{11}	56.9
23.	$2CO(s) \rightarrow C(s) + CO_2(s)$	–	–	1.0×10^{11}	0.0	1.0×10^{11}	129.7
24.	$CH(s) + O(s) \rightarrow CO(s) + H(s)$	–	–	1.0×10^{11}	0.0	1.0×10^{11}	336.8
25.	$CH_3(s) + Pt(s) \rightarrow CH_2(s)s + H(s)$	1.0×10^{13}	20.0	5.0×10^{12}	107.9	1.0×10^{11}	25.5
26.	$CH_3(s) + O(s) \rightarrow CH_2(s)s + OH(s)$	–	–	1.0×10^{11}	84.5	1.0×10^{11}	52.3
27.	$CH_3(s) + OH(s) \rightarrow CH_2(s)s + H_2O(s)$	–	–	1.0×10^{11}	77.8	1.0×10^{11}	21.3
28.	$CH_2(s)s + Pt(s) \rightarrow CH(s) + H(s)$	1.0×10^{13}	20.0	1.0×10^{11}	104.6	1.0×10^{11}	51.0
29.	$CH_2(s)s + OH(s) \rightarrow CH(s) + H_2O(s)$	–	–	1.0×10^{11}	81.6	1.0×10^{11}	55.2
30.	$CH_2(s)s + O(s) \rightarrow CH(s) + OH(s)$	–	–	1.0×10^{11}	83.3	1.0×10^{11}	80.8
31.	$CH(s) + Pt(s) \rightarrow C(s) + H(s)$	1.0×10^{13}	20.0	1.0×10^{11}	22.6	1.0×10^{11}	157.3
32.	$CH(s) + OH(s) \rightarrow C(s) + H_2O(s)$	–	–	1.0×10^{11}	0.4	1.0×10^{11}	159.4
33.	$CH(s) + O(s) \rightarrow C(s) + OH(s)$	–	–	1.0×10^{11}	6.3	1.0×10^{11}	192.0

conservative over the range 4 bar $\leqslant p \leqslant$ 6 bar and GRI-3.0 [31], which was very conservative over the entire pressure range.

The CHEMKIN database was used for the gas-phase thermochemical [33] and transport properties [23]. Gas-phase and surface reaction rates were evaluated with CHEMKIN [34] and Surface-CHEMKIN [35], respectively. A set of hetero/homogeneous schemes will be further denoted by the assigned names of its components: for example, Deutschmann/Warnatz schemes. Finally, the suffix (s) will denote a surface species and the prefix S or R a reaction of the full and the reduced catalytic schemes, respectively.

4. Results and discussion

4.1. Contribution of the gaseous reaction pathway

The importance of the homogeneous reaction pathway and its impact on the assessment of the catalytic reactivity are addressed first. Computed streamwise profiles of both catalytic and gaseous methane conversions are illustrated in Fig. 3 for three cases of Table 1 and two different hetero/homogeneous reaction schemes: Deutschmann/Warnatz and Deutschmann/GRI-3.0. The volumetric gaseous CH_4 conversion rates of Fig. 3 have been integrated across the 7-mm transverse distance, so that they could be di-

Table 2 (*Continued*)

		Deutschmann[b]		Vlachos[c]			
		$A\,(\gamma)$	E	$A_f\,(\gamma)$	E_f	A_b	E_b
Desorption reactions							
34.	$CH_3(s) + H(s) \rightarrow CH_4 + 2Pt(s)$	–	–	1.0×10^{11}	23.0	–	–
35.	$2O(s) \rightarrow O_2 + 2Pt(s)$	1.0×10^{13}	$213.2\text{–}60\theta_O$	1.0×10^{13}	$213\text{–}133.9\theta_O$	–	–
36.	$CH_3(s) \rightarrow CH_3 + Pt(s)$	–	–	1.0×10^{13}	159.0	–	–
37.	$CH_2(s)s \rightarrow CH_2 + Pt(s)$	–	–	1.0×10^{13}	284.5	–	–
38.	$CH(s) \rightarrow CH + Pt(s)$	–	–	1.0×10^{13}	405.8	–	–
39.	$C(s) \rightarrow C + Pt(s)$	–	–	1.0×10^{13}	627.6	–	–
40.	$2H(s) \rightarrow H_2 + 2Pt(s)$	1.0×10^{13}	$67.4\text{–}6\theta_H$	1.0×10^{13}	$83.7\text{–}25.1\theta_H$	–	–
41.	$H(s) \rightarrow H + Pt(s)$	–	–	1.0×10^{13}	$251.9\text{–}20.1\theta_H$	–	–
42.	$O(s) \rightarrow O + Pt(s)$	–	–	1.0×10^{13}	$387.4\text{–}107.1\theta_O$	–	–
43.	$H_2O(s) \rightarrow H_2O + Pt(s)$	1.0×10^{13}	40.3	1.0×10^{13}	41.8	–	–
44.	$OH(s) \rightarrow OH + Pt(s)$	1.0×10^{13}	192.8	1.0×10^{13}	$263.6\text{–}138.1\theta_O$	–	–
45.	$CO_2(s) \rightarrow CO_2 + Pt(s)$	1.0×10^{13}	20.5	1.0×10^{13}	71.1	–	–
46.	$CO(s) \rightarrow CO + Pt(s)$	1.0×10^{13}	125.5	1.0×10^{13}	$142.3\text{–}62.8\theta_{CO}$	–	–

[a] In all pure surface and desorption reactions, the reaction rate coefficient is $k = AT^b \exp(-E/RT)$ with $b = 0$. The units are $A\,(s^{-1})$ and E (kJ/mol) yielding reaction rates in (s^{-1}); to convert to standard surface reaction rate units (mol/cm^2 s), A must be multiplied by Γ^{1-m} where m is the reaction order. In all adsorption reactions A denotes a sticking coefficient (γ), except in Deutschmann's reaction S3, where $k = AT^b \exp(-E/RT)$ with $b = -0.5$ and A in $(mol^{-1}\,cm^3\,K^{0.5}\,s^{-1})$; A in S3 must be multiplied by $1/\Gamma$ to convert to standard surface rate units.

[b] Reactions S2 and S3 are duplicate. Reactions S1, S8, and S14 have a Pt order of 2.3, 1, and 2, respectively.

[c] Parameters are given for the forward (f) and, when appropriate, for the reverse (b) reactions. The activation energies of the adsorption and pure surface reactions are valid for an uncovered surface $(\theta_{Pt} = 1)$; at other surface coverage, they were calculated using BOC (bond order conservation) formulae considering interactions of heats of chemisorption, according to Ref. [7].

rectly compared to the catalytic surface rates; the latter referred to the combined contribution of the upper and lower catalytic surfaces. The onset of appreciable gaseous CH_4 conversion, defined as the position where the gaseous conversion amounted to 5% of the corresponding catalytic conversion (shown with the vertical arrows in Fig. 3), occurred farther upstream in the Deutschmann/GRI-3.0 compared to the Deutschmann/Warnatz schemes. In the former reaction schemes, the gaseous methane conversion overtook the corresponding catalytic conversion shortly after the onset of the appreciable gaseous conversion (see, for example, Figs. 3b and 3c). Moreover, contrary to the OH-LIF experiments, the Deutschmann/GRI-3.0 predictions resulted in the establishment of flames anchored at $x = 140$, 119, and 138 mm for Cases 1, 13, and 15 of Fig. 3, respectively. On the other hand, the Deutschmann/Warnatz schemes captured correctly the absence of flame formation. The performance of GRI-3.0 at the low temperatures relevant to catalytic combustion has been attributed to an unreasonably fast radical pool buildup that resulted in a rapid methane depletion, predominantly via the step $CH_4 + OH = CH_3 + H_2O$ (see discussion in Reinke et al. [3]). The computations of Fig. 3 were repeated with the scheme of Vlachos replacing that of Deutschmann; the onset of appreciable gaseous conversion shifted farther downstream, the

reason being that the former catalytic scheme was—as discussed in the next section—considerably faster than the latter and could, therefore, suppress more effectively the contribution of the gaseous pathway by depriving it from fuel. The previous analysis with different hetero/homogeneous schemes aimed at delineating the streamwise extent of the channel that had negligible gas-phase participation and was, therefore, suitable for catalytic reactivity studies. Notwithstanding the known deficiencies of GRI-3.0, the most conservative estimate was chosen by considering the length of the channel down to the position of appreciable gaseous conversion as computed with the Deutschmann/GRI-3.0 schemes. For the investigation of the hetero/homogeneous processes downstream of this position, however, only predictions with the realistic scheme of Warnatz will be presented.

The measured surface temperature profiles of both upper and lower catalytic plates are presented in Fig. 4 for seven selected cases of Table 1. Since the gaseous reactivity of hydrocarbons increased with increasing pressure [36], the surface temperatures were, in general, reduced at higher pressures in order to suppress the gaseous contribution and the onset of homogeneous ignition. The increased gaseous reactivity of CH_4 at elevated pressures could be readily seen by comparing Figs. 3a and 3b: although the Reynolds numbers and the inlet temperatures of Cases 1 (4 bar)
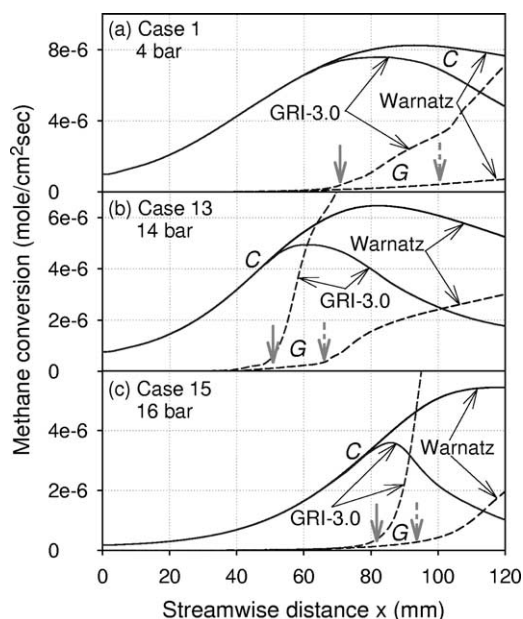
Fig. 3. Computed streamwise profiles of catalytic (C: solid lines) and gaseous (G: dashed lines) methane conversions for (a) Case 1, (b) Case 13, and (c) Case 15 of Table 1; the G conversions have been integrated over the channel transverse direction. The computations refer to the Deutschmann/Warnatz and Deutschmann/GRI-3.0 reaction schemes. The onset of appreciable gaseous methane conversion (defined as the point where the gaseous conversion amounts to 5% of the catalytic conversion) is indicated by the dashed vertical arrow in the former schemes and by the solid vertical arrow in the latter.

Fig. 4. Measured streamwise profiles of surface temperatures for seven selected cases of Table 1. Solid lines, lower catalytic wall; dotted lines, upper wall. The vertical tick marks on the horizontal axis indicate the thermocouple positions on both catalytic walls.

and 13 (14 bar) were about the same (indicating a nearly equivalent reactor mass throughput), the onset of appreciable gaseous conversion was located, irrespective of gaseous scheme, farther upstream in Case 13 compared to Case 1. Moreover, this happened despite the fact that Case 13 had (compared to Case 1) lower surface temperatures (see Fig. 4) and higher upstream catalytic conversions (see Fig. 3) that led to reduced fuel availability for the gaseous pathway. Case 15 (16 bar) had also about the same mass throughput as Cases 1 and 13; however, its surface temperatures were sufficiently low (Fig. 4) and this effect overtook the positive pressure dependence of the gaseous reactivity. An additional reason for the reduction of the surface temperatures with increasing pressure was an—similar to the gas phase—increase of the catalytic reactivity with increasing pressure (see discussion in next section), which shifted the catalytic conversion close to the undesirable mass-transport-limited operation.

The measured boundary-layer profiles of the deficient reactant (methane) were of main interest for the assessment of the catalytic reactivity. The experimental requirements for such a task are discussed with the aid of Fig. 5, referring to the three 16-bar cases of Table 1. Case 14 had the lowest surface temperatures (Fig. 4) that resulted in a minimal catalytic reactivity, as manifested by the nearly flat and featureless measured methane boundary-layer profiles down to $x = 93.5$ mm (Fig. 5b). Although such profiles were of limited interest, they nevertheless exemplified the large differences between the two heterogeneous schemes; the scheme of Vlachos was considerably faster than the scheme of Deutschmann, the latter being in relatively good agreement with the measurements as will be further elaborated in the next section. The onset of appreciable gaseous conversion (according to the adopted conservative definition) in Case 14 was located at $x = 102$ mm. Therefore, the predictions of Figs. 5a and 5b were totally unaffected by the choice of gaseous scheme (GRI-3.0, Warnatz, or no gaseous scheme at all) and reflected solely the influence of the catalytic pathway—albeit with a diminishing impact. The surface temperatures in Case 15 were high enough as to induce at downstream locations (Fig. 5d, $x = 113.5$ mm) a bending in the measured CH_4 boundary-layer profile, which was cardinal in assessing the catalytic reactivity. Fortuitously, the CH_4 boundary-layer profiles appeared largely unaffected by the presence of gaseous reactions (except in the wall proximity where the transverse gradient of CH_4 determined the magnitude of the local catalytic
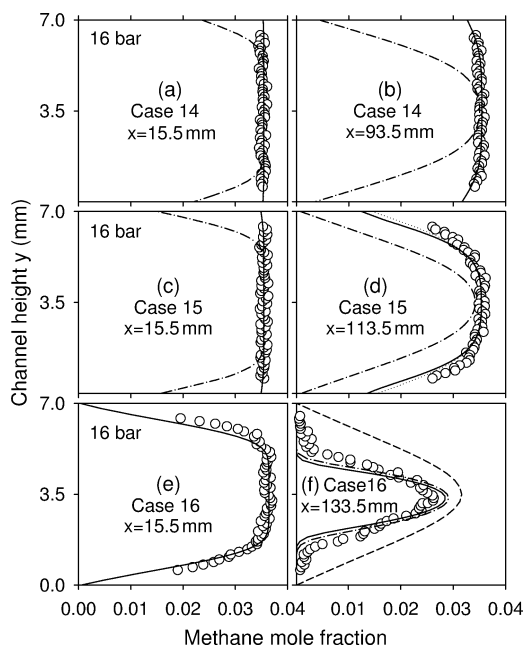
Fig. 5. Measured and predicted transverse profiles of the methane mole fractions at two selected streamwise distances for the three 16-bar cases of Table 1. Symbols are measurements and lines are predictions. Circles, Raman measurements; solid lines, predictions with Deutschmann/Warnatz schemes; dashed-dotted lines, predictions with Vlachos/Warnatz schemes. In (d) the dotted lines are pure heterogeneous predictions with the Deutschmann scheme (no gaseous chemistry), in (e) the Deutschmann/Warnatz and Vlachos/Warnatz predictions coincide, and in (f) the dashed lines pertain to two coinciding purely heterogeneous predictions with the Deutschmann and Vlachos schemes. In (e) the catalytic reactions are mass-transport limited, whereas in (f) the methane profile is largely determined by the gaseous reaction pathway due to the presence of a flame in the reactor.

conversion), even at positions downstream of the onset of appreciable gaseous conversion. In Fig. 5d, for example, predictions with the Deutschmann/Warnatz schemes (solid line) were in good agreement with those using only Deutschmann's scheme without gaseous chemistry (dotted line), despite the fact that the gaseous methane conversion in the former predictions amounted already to 18% of the catalytic conversion at $x = 113.5$ mm (see Fig. 3c). The reason was that the gaseous pathway suppressed the catalytic conversion (see the drop of the C curves upon the rise of the G curves in Fig. 3) in such a way that the sum of catalytic and gaseous conversions was close to the pure catalytic conversion attained in the absence of gaseous chemistry; in Case 13, for example, the computed total fractional CH_4 conversion $(= [\dot{m}_{CH_4,IN} - \dot{m}_{CH_4}(x)]/\dot{m}_{CH_4,IN})$ at $x = 120$ mm was 16.6% (12.4% catalytic and 4.2% gaseous) with

the Deutschmann/Warnatz schemes and 15.1% pure catalytic with the Deutschmann scheme alone. This fortuitous agreement, however, by no means suggested the use of positions downstream of the designated onset of appreciable gaseous conversion for the assessment of the catalytic reactivity. The CH_4 profiles of Figs. 5a–5d exhibited only a slight asymmetry since the temperature differences between upper and lower walls were less than 12 K at any axial position of Case 14 or 15 (see Fig. 4).

Case 16 (Figs. 5e and 5f) had the highest surface temperatures and a flame anchored at $x \approx 115$ mm, as determined by the OH-LIF experiments and also captured well by the Deutschmann/Warnatz schemes. Even though the onset of appreciable gaseous conversion occurred at $x = 20$ mm, the measurements at $x = 15.5$ mm (Fig. 5e) were of very limited use since the catalytic conversion was already mass-transport limited, as manifested by the predicted nearly zero CH_4 concentrations at both walls. The computations of both Deutschmann and Vlachos schemes (with or without the inclusion of any of the two gaseous schemes) coincided in Fig. 5e; however, no kinetic information could be extracted under such operating conditions. The position of Fig. 5f was well downstream of the onset of homogeneous ignition, as also evidenced by the absence of CH_4 in extended regions close to both channel walls. When the gaseous scheme was removed, the pure heterogeneous predictions of both Deutschmann and Vlachos schemes coincided (dashed line in Fig. 5f), the catalytic conversion being again mass-transport limited. The discussion of Fig. 5 has exemplified the importance of operating conditions that ensured methane profiles similar to those of Case 15. Finally, it is noted that the surface temperature provided the prime means of controlling the bending of the CH_4 boundary-layer profiles. An alternate approach would have been to vary the transport by altering the inlet Reynolds numbers; nevertheless, the CH_4 boundary-layer profiles were much less responsive to Reynolds number changes.

To understand the coupling between the heterogeneous and homogeneous pathways, reaction flux analyses were carried out for different cases of Table 1, at various streamwise positions. The gaseous and catalytic carbon fluxes (predicted with the Deutschmann/Warnatz schemes) for Case 13 (14 bar) at $x = 95$ mm are presented in Fig. 6; the gas-phase fluxes were obtained by integrating the volumetric gaseous reaction rates over the 7-mm transverse direction and the surface fluxes referred to the contribution of both catalytic walls. Similar flux analyses revealed that all the important reaction routes of Fig. 6 remained unaffected by pressure over the entire range 4 bar $\leqslant p \leqslant$ 16 bar. At $x = 95$ mm the
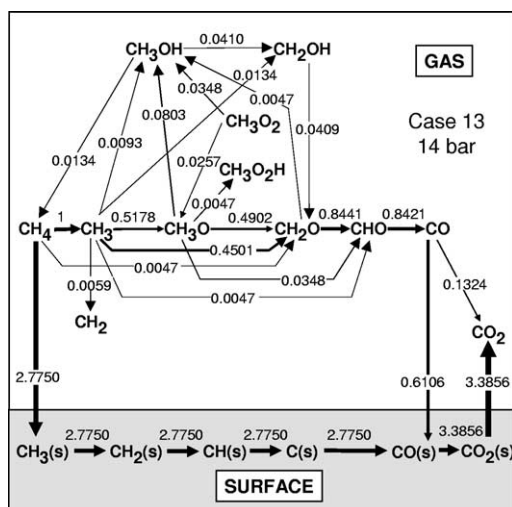
Fig. 6. Homogeneous and heterogeneous reaction flux analysis for Case 13 (14 bar) at $x = 95$ mm computed with the Deutschmann/Warnatz reaction schemes. All fluxes are normalized with respect to the flux of the gaseous reaction $CH_4 \rightarrow CH_3$; only fluxes with relative magnitude greater than 0.004 are shown. The gaseous fluxes have been obtained by integrating the volumetric gaseous reaction rates over the channel transverse direction.
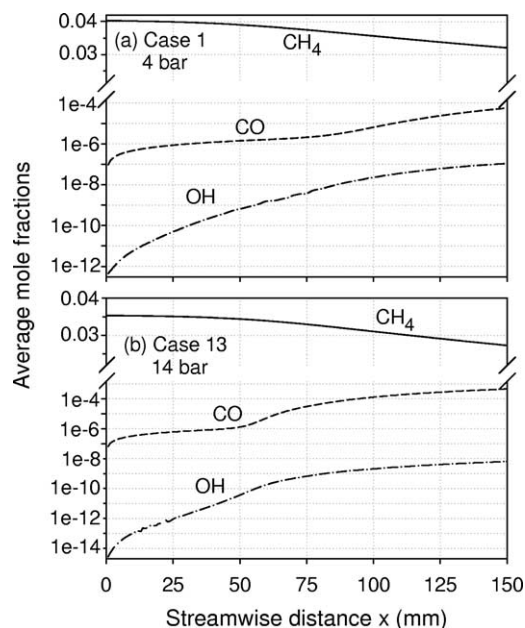
Fig. 8. Computed streamwise profiles of the average (over the channel transverse direction) mole fractions of CH_4, CO, and OH for (a) Case 1 and (b) Case 13; the Deutschmann/Warnatz reaction schemes were used in the computations.
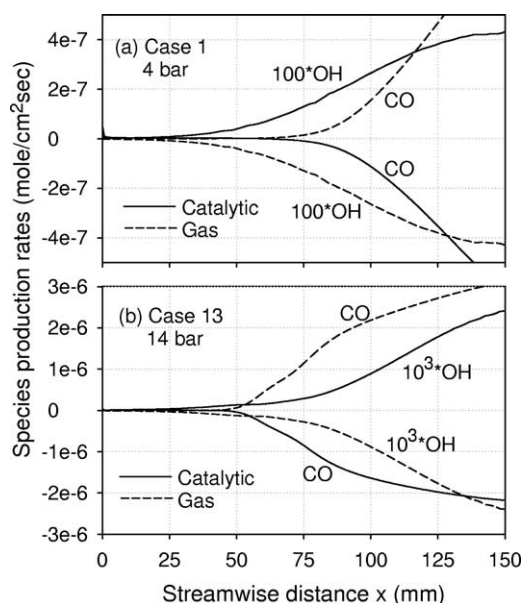
Fig. 7. Computed streamwise profiles of the catalytic (solid lines) and the gaseous (dashed lines) production rates of CO and OH obtained with the Deutschmann/Warnatz reaction schemes: (a) Case 1 (4 bar) and (b) Case 13 (14 bar). The gaseous reaction rates have been integrated over the channel transverse distance. In both cases, the OH (CO) is produced (destroyed) by the catalytic pathway and destroyed (produced) by the gaseous pathway.

gaseous methane conversion amounted to 36% of the corresponding catalytic conversion (see also Fig. 3b). The gaseous pathway converted CH_4 predominantly to CO, the initiating step in the methane breakup being always $CH_4 + OH = CH_3 + H_2O$. Most of the formed CO was adsorbed on the catalyst and only a small fraction of it was oxidized to CO_2 in the gas phase. The adsorbed CO was subsequently oxidized on the surface to $CO_2(s)$, which, along with the $CO_2(s)$ produced via the main methane surface oxidation route, desorbed back to the gas phase as CO_2. Streamwise profiles of the production rates of CO and OH and the mole fractions of CH_4, CO, and OH for Case 13 are illustrated in Figs. 7b and 8b, respectively; the gas-phase rates of Fig. 7 have been integrated over the 7-mm transverse distance and the mole fractions of Fig. 8 have been averaged over the same distance. Using the streamwise profiles of Fig. 8b, a fractional CH_4 conversion of 23% could be deduced at $x = 150$ mm; 16% was catalytic and 7% gaseous. The gaseous and catalytic pathways produced and destroyed, respectively, CO (see Fig. 7b), with a positive net production that resulted in the attained low CO levels along the channel length (see Fig. 8b). For the very fuel-lean conditions of this study, the removal of both CO adsorption and desorption reactions resulted only in a moderate increase of the CO levels (in Case 13, for example, the CO

mole fraction increased from 5×10^{-4} to 1.2×10^{-3} at $x = 150$ mm) since the oxidation of CO to CO_2 was rerouted efficiently from the catalytic to the gaseous pathway. This outcome will be used in the forthcoming reduction of the heterogeneous scheme of Deutschmann.

The hetero/homogeneous radical coupling is addressed next. The OH radical was produced by the catalytic pathway (the net OH heterogeneous flux was desorptive) and destroyed by the gaseous pathway (see Fig. 7b); the catalytic production rate was somewhat larger than the gaseous destruction rate, resulting in the streamwise increase of the OH mole fraction shown in Fig. 8b. It would, therefore, appear that the catalytically produced OH promoted gaseous conversion by accelerating the main fuel attack step $CH_4 + OH = CH_3 + H_2O$. However, the net OH heterogeneous fluxes were too low to have an appreciable impact on the gas-phase pathway and, consequently, on the flux analysis of Fig. 6. This was also verified by removing the OH adsorption and desorption reactions from the scheme of Deutschmann and computing anew: the CH_4 gas conversion of Fig. 3b and the CH_4, CO, and OH levels of Fig. 8b remained virtually unaffected. The gaseous chemistry was still able to build the radical pool without the aid of the heterogeneous pathway. In other words, the catalyst itself was a very poor source of OH as to meaningfully affect the gaseous pathway under conditions away from homogeneous ignition and flame propagation. In the presence of a flame or at the late prehomogeneous-ignition stages, however, the catalyst could become a very efficient sink of gas-produced OH, inhibiting gaseous combustion (see also [3,25]). A similar analysis has shown that the catalytic and gaseous coupling of both O and H radicals was minimal, a conclusion valid not only under the conditions of this study but also during homogeneous ignition and flame propagation (see also the atmospheric-pressure studies in [25]). The above discussion on the hetero/homogeneous chemistry coupling applied, qualitatively, at all pressures; Figs. 7a and 8a of Case 1 (4 bar) exhibited the same trends as their 14-bar counterparts of Figs. 7b and 8b. It is finally noted that, for a fixed reactor pressure and surface temperature, the contribution of the gaseous pathway was controlled primarily by the reactor surface-to-volume ratio (SV) and residence time (τ); an increase (decrease) in SV (τ) could suppress effectively the gaseous contribution. The channel-flow reactor of Fig. 1 had a relatively small $SV = 2.86$ cm^{-1}. The delineation of the SV–τ regimes leading to an appreciable gas-phase contribution will be dealt in the forthcoming section on reduced schemes.

4.2. Comparisons between measurements and predictions and effect of pressure on catalytic reactivity

Measured and predicted—using both Deutschmann and Vlachos heterogeneous schemes—transverse profiles of the CH_4 and H_2O mole fractions and of the temperature are presented in Fig. 9 for five selected cases of Table 1 and four streamwise positions for each case. All predicted profiles of Fig. 9 were totally unaffected by the presence of gaseous chemistry, as they referred to axial positions before the onset of appreciable gaseous conversion. The slight-to-moderate asymmetry in both measured and predicted profiles of Fig. 9 was ascribed to the varying degree of temperature difference between the catalytic plates, the lower plate being usually the hottest one (see Fig. 4). The CH_4 levels in Fig. 9 ranged from 2 to 4% per volume over the exploitable transverse extent of the experiments (0.6 mm $\leqslant y \leqslant$ 6.4 mm), resulting in a measurement accuracy of $\pm 5\%$. Over the same transverse extent, the H_2O levels ranged from practically zero about the symmetry plane ($y = 3.5$ mm) of all upstream axial positions, to 2.5% per volume at the end measurement points $y = 0.6$ mm and $y = 6.4$ mm. An accuracy of $\pm 10\%$ was attained in the near wall regions with H_2O volumetric concentrations greater than 0.5%; the lower H_2O concentrations about the channel center resulted in poor accuracy; however, these regions were of little interest in the present analysis. The H_2O measurements complemented the CH_4 ones and aided the scheme validation process, since the near-wall rise of H_2O was directly linked to the catalytic conversion of CH_4. The O_2 Raman data were of less importance since this reactant was in excess, having a boundary-layer profile with a weak near-wall bending. It should be pointed out that in situ, spatially resolved measurements of species compositions over a catalyst (such as those of Fig. 9) under high pressure have not been reported in the literature.

The measured and predicted CH_4 and H_2O boundary-layer profiles were compared against each other in order to assess the performance of the heterogeneous schemes. The scheme of Vlachos overpredicted at all pressures the catalytic reactivity as it resulted in significantly lower (higher) near-wall CH_4 (H_2O) levels. The scheme of Deutschmann, on the other hand, yielded an overall good agreement with the experiments at all pressures. The catalytic reactivity appeared to be slightly overpredicted in Deutschmann's scheme: the computed CH_4 drop and the H_2O rise near the wall were somewhat faster compared to the measurements. The above discrepancies were, however, within the experimental uncertainty. The proper choice of surface temperatures has exemplified the
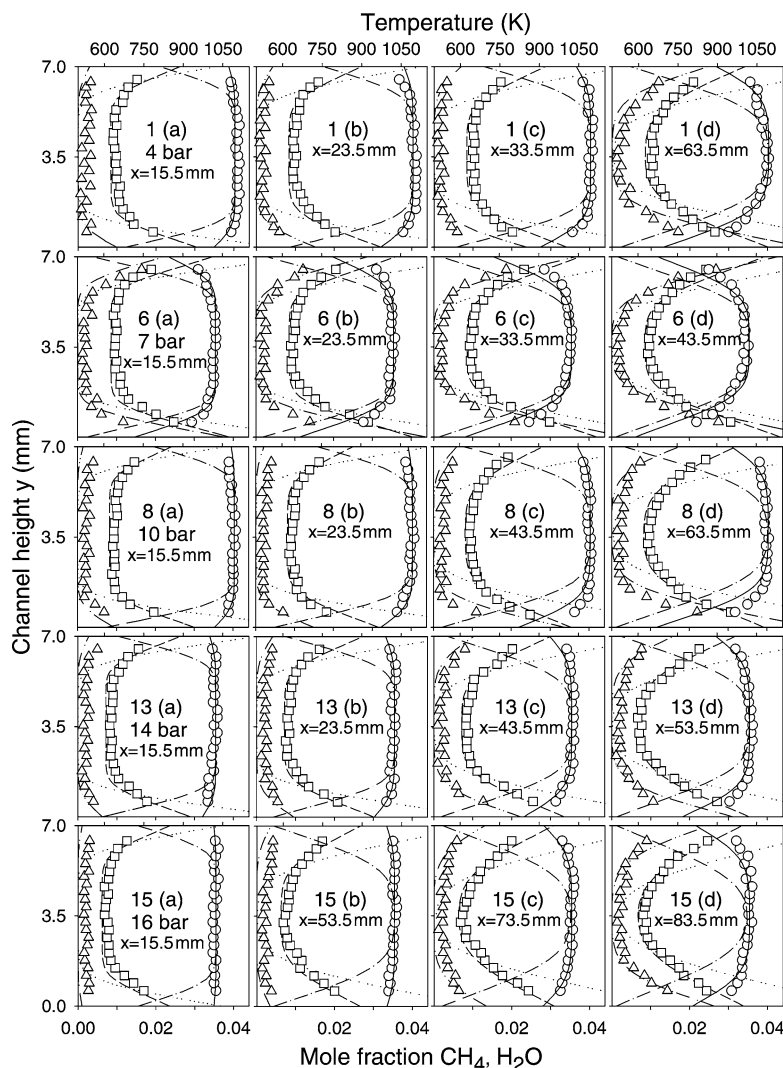
Fig. 9. Comparisons between measured and predicted transverse profiles of temperature and species (CH_4 and H_2O) mole fractions for five cases of Table 1. Four streamwise locations are presented for each case. Measurements: CH_4 (circles), H_2O (triangles), and temperature (squares). Predictions: CH_4 (solid line, Deutschmann/Warnatz schemes; dashed-dotted lines, Vlachos/Warnatz schemes) and H_2O (dashed-double-dotted lines, Deutschmann/Warnatz schemes; dotted lines, Vlachos/Warnatz schemes). The predicted temperature profiles with the Deutschmann/Warnatz and Vlachos/Warnatz schemes coincided (dashed lines). For reasons of clarity, 21 of the 63 transverse measurement points are shown.

large differences between the two reaction schemes. For example, in Case 6 that had the highest surface temperatures of all cases of Fig. 9 (see Fig. 4), the differences between the two predictions was moderate already from the first axial position $x = 15.5$ mm. Notwithstanding the large differences between the two scheme predictions in their corresponding CH_4 and H_2O profiles, the predicted temperature profiles were practically coincident. The reason was that the surface temperatures were prescribed in the computations of both schemes and that the changes in the thermal conductivity and heat capacity of a partially re-

acted fuel-lean methane/air premixture were, largely, independent of the progress of the reaction. The following analysis will focus on the validated heterogeneous scheme of Deutschmann.

The effect of pressure on the catalytic reactivity is elaborated with the aid of Figs. 9 and 10a. Figure 10a pertains to computations of a surface perfectly stirred reactor (SPSR) [37] using the scheme of Deutschmann (no gaseous scheme included) and three different pressures: 1, 4, and 16 bar. The surface to volume ratio (*SV*) in the SPSR computations was 2.86 cm^{-1} (equal to the channel *SV*) and the
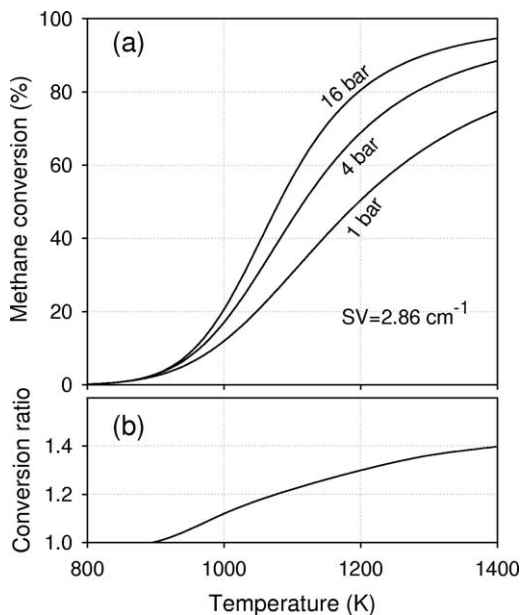
Fig. 10. (a) Computed heterogeneous (using the scheme of Deutschmann without inclusion of gaseous chemistry) in a surface perfectly stirred reactor (SPSR) at three different pressures. The surface to volume ratio is 2.86 cm^{-1}, the equivalence ratio is $\varphi = 0.4$, and the residence times are 10, 40, and 160 ms at 1, 4, and 16 bar, respectively. (b) SPSR predictions of the ratio of the methane catalytic conversion at 16 bar to that at 4 bar. The residence times at 4 bar are such that the methane conversion is always 50% and the residence times at 16 bar are a factor of 4 longer compared to those at 4 bar.

Fig. 11. Computed profiles of the surface coverage (referring to the lower catalyst surface) for (a) Case 1 and (b) Case 13. Solid lines, Deutschmann/Warnatz schemes; dotted lines, Vlachos/Warnatz reaction schemes.

residence times were increased proportionally with increased pressure in order to maintain equal SPSR mass-flow rates; this mimicked the channel-flow experiments of Fig. 9 that had a nearly constant mass throughput. The SPSR residence times at 4 and 16 bar were 40 and 160 ms, respectively, which—using the flow velocities of Table 1—corresponded to an equivalent reactor length of about 80 mm. The influence of pressure on catalytic reactivity could be deduced directly from the SPSR predictions or with appropriate profile comparisons in Fig. 9. For example, Figs. 9(1b) and 9(8b) indicated that the bending of the measured CH$_4$ (as well as H$_2$O) profiles near both walls was roughly the same: given the fact that the transverse fluid mechanical transport was nearly the same in both cases (for a given x it scaled with Re_{IN} as discussed in Refs. [17,26]), this entailed nearly equivalent catalytic reaction rates for both cases according to the diffusion-reaction interfacial balance of Eqs. (9). Since the surface temperatures were lower in the higher pressure Case 8 compared to Case 1 (by 40 and 10 K in the upper and lower surfaces, respectively, see Fig. 4), this necessitated

an increase of the catalytic reactivity with increasing pressure. The same conclusion could be readily reached with the SPSR computations of Fig. 10a: predictions with the scheme of Deutschmann indicated that the catalytic reactivity increased with pressure as manifested by the corresponding higher methane conversions. Moreover, the increase in the catalytic reactivity with increasing pressure was more pronounced at higher temperatures. This was shown with additional SPSR calculations where the residence times at 4 bar were altered independently as to achieve a fixed 50% methane conversion at various temperatures. The corresponding methane conversions were then calculated at 16 bar, using residence times that were a factor of 4 longer than those computed at 4 bar (to maintain the same reactor mass throughput). The ratio of the 16-to-4 bar conversions is illustrated in Fig. 10b, clearly showing the weaker pressure dependence of the catalytic reactivity at lower temperatures.

The origin of the differences between the two reaction schemes and the impact of pressure on the catalytic reactivity is elaborated with the surface coverage of Fig. 11, referring to the lower catalytic surfaces of Cases 1 and 13. The initiation step in both schemes was the dissociative adsorption of methane (reaction S1): CH$_4$ + 2Pt(s) → CH$_3$(s) + H(s). In the scheme of Deutschmann S1 had an order of 2.3 with respect to Pt, so that the adsorption rate of CH$_4$ was

$$\dot{s}_{\text{ads,CH}_4} = k_{\text{ads,CH}_4}[\text{CH}_4][\Gamma\theta_{\text{Pt}}]^{2.3}, \qquad (12)$$

with k_{ads,CH_4} given in Eq. (11). The main surface coverage was O(s) and free sites (Pt(s)) as seen in Fig. 11. For a given case and reaction scheme, the O(s) dropped with increasing x due to the corresponding increase of the surface temperature (see Fig. 4), which promoted the desorption of O(s) and the creation of free sites. As the pressure increased, the corresponding increase in the O_2 partial pressure resulted in further adsorption of O_2 and hence to higher O(s) and lower Pt(s) coverage for both reaction schemes (see Fig. 11); in the scheme of Deutschmann, however, the reduction of the Pt(s)/O(s) ratio with increasing pressure was much more pronounced. It is emphasized that the Pt(s) and O(s) differences between Figs. 11a and 11b reflected the effect of pressure and not the (small) differences in surface temperatures $T_W(x)$ and φ; this was verified by replacing $T_W(x)$ and φ of Case 13 with those of Case 1 and computing anew. To facilitate the ensuing discussion, the drop of θ_{Pt} with increasing pressure will be represented as $[\theta_{Pt}] \propto p^{-\beta}$, with β a positive number that need not be a constant but a function of local parameters such as surface temperature and coverage. As seen in Eq. (12), the methane adsorption rate was a product of the positive $[CH_4] \propto p$ gas-phase concentration dependence and the negative p^{-n} surface coverage dependence (in Deutschmann's scheme $n = 2.3\beta$). The exponent n was always smaller than unity, such that the catalytic reactivity had a positive pressure dependence p^{1-n}, the specific value of n being very important in *restraining* the rate of increase of the catalytic reactivity with increasing pressure. The above pressure dependence was also recognized in earlier empirical global reaction steps [38] proposed for engineering applications,

$$\dot{s}_{CH_4} = Bp^{-n} \exp(-E_a/RT)[CH_4], \qquad (13)$$

with a constant exponent $n = 0.4$ and $E_a = 77$ kJ/mol. The scheme of Deutschmann appeared to have the proper local pressure inhibition through the p^{-n} term that resulted in the capture of the pressure dependence of the catalytic reactivity. Interestingly, the $\dot{s}_{ads,CH_4} \propto [\theta_{Pt}]^{2.3}$ dependence in Deutschmann's scheme that was, in turn, responsible for the capture of the correct local exponent n was derived from atmospheric pressure experiments; its apparent validity at pressures as high as 16 bar is worth noting.

A heterogeneous reaction flux analysis for Case 13 at $x = 95$ mm is shown in Fig. 12; the fluxes were calculated with the Deutschmann/Warnatz reaction schemes and referred to the lower catalyst surface. Flux analyses of different cases have revealed that the dominant pathways of Fig. 12 were unaffected by pressure. The initiating step was the dissociative adsorption of CH_4 to H(s) and C(s) and of O_2 to O(s), the main surface steps were the reaction of
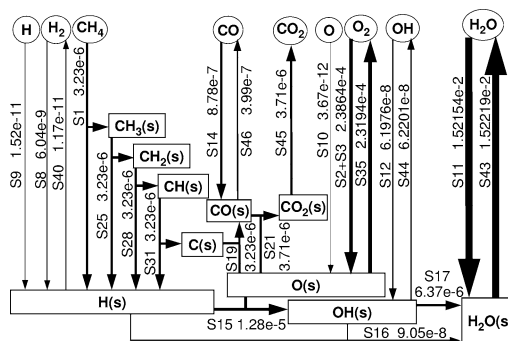
Fig. 12. Heterogeneous reaction flux analysis (the units are mol/cm^2 s) for Case 13 (14 bar) at $x = 95$ mm, referring to the lower catalytic plate. The Deutschmann/Warnatz reaction schemes were used.

O(s) with H(s) and C(s) to form OH(s)/H_2O(s) and CO(s)/CO_2(s), respectively, and, finally, the desorption of H_2O(s) and CO_2(s) led to the main gaseous products H_2O and CO_2. The dominant pathways were also the same in the scheme of Vlachos and are not shown here. There were differences in the order of significance of certain surface pathways; for example, H_2O(s) in Deutschmann's scheme was produced primarily via S17 whereas in Vlachos' scheme via S16. However, the above differences were not crucial for the overall scheme behavior. The performance differences of the two schemes shown in Figs. 5 and 9 reflected strongly differences between the CH_4 and O_2 adsorption/desorption reactions: the relative magnitude of these two steps determined the dominant Pt(s) and O(s) coverage and, hence, the resulting catalytic reactivity inhibition through the aforementioned p^{-n} dependence. When only the O(s) desorption (reaction S35) of Vlachos' scheme was interchanged with the corresponding one of Deutschmann's scheme, the computed SPSR conversions of the former scheme were improved significantly, particularly at $T < 1100$ K. The reason was that the activation energy of S35 in Vlachos' scheme had a much stronger dependence on the O(s) coverage (see Table 2), which resulted in a more efficient O(s) desorption and, therefore, in a higher Pt(s) coverage and in a higher catalytic reactivity (smaller value of the exponent n). When all the CH_4 and O_2 adsorption and desorption reactions of Vlachos' scheme were interchanged with the corresponding ones of Deutschmann's scheme, the SPSR predictions of both schemes coincided.

4.3. Reduced heterogeneous schemes

It is of main interest to provide reduced heterogeneous reaction schemes that could predict accurately the catalytic methane conversion. Moreover, when
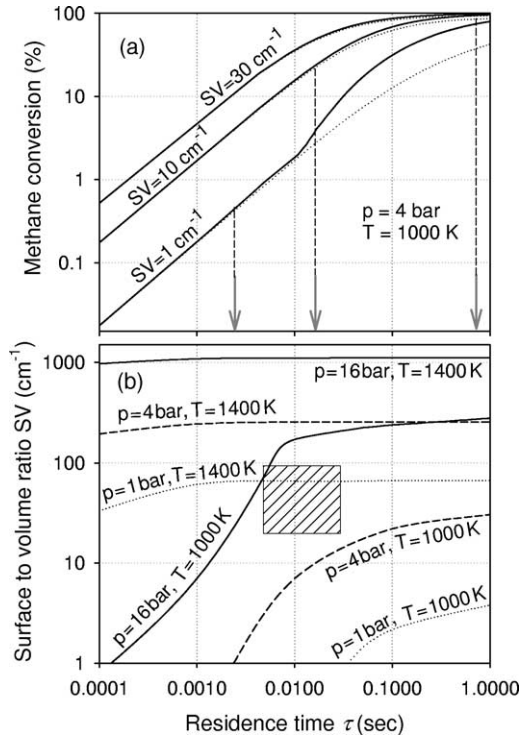
Fig. 13. (a) Computed methane conversions in a surface perfectly stirred reactor (SPSR) with the Deutschmann/Warnatz reaction schemes and $\varphi = 0.4$: the solid lines are the total (gaseous and catalytic) conversions and the dotted lines the catalytic conversions. The onset of gaseous conversion (shown with the vertical arrows) is favored at longer residence times (τ) or smaller surface-to-volume (SV) ratios. (b) Delineation of the regimes of significant gas-phase chemistry participation. For a given reactor pressure and temperature the area above each line delineates the τ and SV regimes for which gas-phase contribution can be neglected; dotted lines, 1 bar; dashed lines, 4 bar; solid lines, 16 bar. The shaded area presents an estimate of the regimes relevant to catalytically stabilized combustion (CST) gas turbine applications.

coupled to the homogeneous scheme of Warnatz, the reduced heterogeneous schemes should predict adequately not only the catalytic but also the gaseous methane conversion—whenever the latter is of importance. The validated elementary heterogeneous scheme of Deutschmann and the gaseous scheme of Warnatz were used in the reduction process: the latter has been shown (in conjunction with the scheme of Deutschmann) to reproduce well the onset of homogeneous ignition in the channel reactor over the pressure range 6 bar $\leqslant p \leqslant$ 16 bar and to underestimate homogeneous ignition only moderately in the range 4 bar $\leqslant p \leqslant$ 6 bar (see the discussion in Section 3.2). The first step in the reduction procedure was the delineation of the parameter range over

which the gaseous pathway could be neglected. SPSR predictions of the total (catalytic plus gaseous) and catalytic methane conversions versus residence time are illustrated in Fig. 13a for various SV's. The vertical arrows defined the maximum allowable reactor residence times: longer residence times resulted in a gaseous conversion that exceeded 5% of the corresponding total conversion. Computations similar to those of Fig. 13a were used to construct the parametric plot of Fig. 13b. The lines in Fig. 13b corresponded to a fixed reactor pressure and temperature; in the regions above each line the gaseous participation could be safely ignored, while in the areas below the gaseous contribution should always be considered. The line leveling in Fig. 13b indicated that, above a certain value of SV (that depended on the reactor pressure and temperature), the maximum allowable residence times were extremely sensitive to small changes in SV. The plot of Fig. 13b was nearly independent of the particular equivalence ratio over the experimental range $0.35 \leqslant \varphi \leqslant 0.40$. The shaded rectangle provided an estimate of the regimes applicable to gas turbines. It is understood that the graph of Fig. 13b (based on ideal reactor predictions) provided a rough delineation of the regimes of significant gas-phase participation. A technical supported catalyst would have a porous substrate with an effective area significantly larger than the geometrical one. This would necessitate modeling of intrapolar diffusion and assessment of its importance by comparing the intrapolar diffusion times with the in-channel convective and diffusion time scales; such issues are, however, outside the scope of this work. The position of the shaded rectangle in Fig. 13b indicated that the gas phase participation could not be neglected at $p \geqslant 16$ bar and $T \geqslant 1000$ K, an operating range that encompasses many practical systems. This was also verified with additional 2-D computations in technically relevant catalytic channel geometries. For example, in a channel with diameter of 2 mm (geometrical $SV = 20$ cm^{-1}), a length of 100 mm, $T_{IN} = 673$ K, $U_{IN} = 5$ m/s (residence time ~20 ms), $p = 16$ bar, and a fixed wall temperature $T_W = 1200$ K, the computations yielded a fractional methane conversion of 45% out of which 6% was gaseous and 39% catalytic; when the channel diameter was reduced to 1 mm with $SV = 40$ cm^{-1} (all other parameters being the same) the total fractional conversion was 84% with 10% gaseous and 74% catalytic contributions.

In the regions of Fig. 13b with insignificant gaseous participation, the sole requirement of the reduced heterogeneous scheme was to reproduce the catalytic methane conversion. The reduction of the scheme of Deutschmann was aided by the reaction flux analysis of Fig. 12 and the sensitivity analysis (SA) of Fig. 14. The SA of Fig. 14 was carried
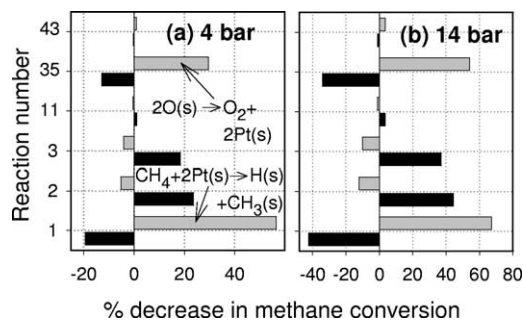
Fig. 14. Sensitivity analysis of the heterogeneous pathway for Cases 1 (4 bar) and 13 (14 bar) of Table 1. The six most sensitive reactions of Table 2 are shown for the heterogeneous scheme of Deutschmann. The percentage reduction in the methane catalytic conversion is computed for an increase (black bars) or decrease (gray bars) of the reaction preexponential coefficient by a factor of 10.

out by multiplying (dividing) the preexponential of each reaction by a factor of 10 and then computing (without inclusion of gaseous chemistry) the catalytic methane conversion along the channel anew. The six most significant reactions are illustrated for each heterogeneous scheme; the order of significance of these reactions remained unaffected by pressure. The most sensitive reactions in both schemes were the adsorption/desorption of CH_4 and O_2, which were the rate-limiting steps. The pure surface reactions were too fast to affect the methane conversion; characteristically, a decrease of the rate of reactions S15 to S33 in Deutschmann's scheme by a factor of 10^3 did not alter appreciably the catalytic conversion. Hence, the consecutive reactions

$$CH_4 \xrightarrow{S1} CH_3(s) \xrightarrow{S25} CH_2(s) \xrightarrow{S28} CH(s)$$
$$\xrightarrow{S31} C(s) + 4H(s)$$
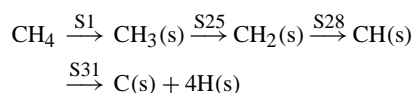
were combined to the single step:

$$CH_4 + 5Pt(s) \rightarrow C(s) + 4H(s). \tag{R1}$$

Reaction R1 had the same kinetic parameters with S1 (the slowest reaction of the chain), including the reaction order of 2.3 with respect to Pt(s).

In the absence of significant gas-phase participation, the radical (OH, O, and H) adsorption/desorption reactions could be ignored. Furthermore, in the absence of H_2 in the reactant stream, the H_2 adsorption/desorption reactions could be removed, as they did not have any noticeable impact on H(s). Water was formed primarily via S17 (see Fig. 12) and, therefore, S16 was disregarded; in any case, inclusion of either S17 or S16 was sufficient to accommodate the water formation given the fact that all surface reactions were much faster compared to the adsorption

Table 3
Reduced heterogeneous scheme[a]

R1	$CH_4 + 5Pt(s) \xrightarrow{S1} C(s) + 4H(s)$
R2	$O_2 + 2Pt(s) \xrightarrow{S2} 2O(s)$
R3	$O_2 + 2Pt(s) \xrightarrow{S3} 2O(s)$
R4	$H_2O + Pt(s) \xrightarrow{S11} H_2O(s)$
R5	$H(s) + O(s) \overset{S15}{=} OH(s) + Pt(s)$
R6	$OH(s) + OH(s) \overset{S17}{=} H_2O(s) + O(s)$
R7	$C(s) + 2O(s) \xrightarrow{S19} CO_2(s) + 2Pt(s)$
R8	$2O(s) \xrightarrow{S35} O_2 + 2Pt(s)$
R9	$H_2O(s) \xrightarrow{S43} H_2O + Pt(s)$
R10	$CO_2(s) \xrightarrow{S46} CO_2 + Pt(s)$
R11	$OH + Pt(s) \xrightarrow{S12} OH(s)$
R12	$OH(s) \xrightarrow{S44} OH + Pt(s)$
R13	$CO + O(s) + Pt(s) \xrightarrow{S14} CO_2(s) + Pt(s)$

[a] The reduced scheme R1–R10 is valid for purely heterogeneous combustion and stems from the full scheme of Deutschmann (see Table 2). The augmented reduced scheme R1–R13 can be used for combined catalytic and gaseous combustion. The reduced reactions (R reactions) have the same kinetic rate parameters to the indicated S reactions of the full scheme of Deutschmann. R1 and R13 have a reaction order with respect to Pt(s) of 2.3 and 2, respectively. R7 and R13 have a reaction order with respect to O(s) of 1 and 0, respectively.

and desorption reactions. Finally, as discussed previously in Section 4.1, under fuel-lean conditions and in the absence of gaseous chemistry, the catalyst was an extremely poor producer of CO; therefore, the adsorption/desorption of CO were ignored and the consecutive surface steps $C(s) \xrightarrow{S19} CO(s) \xrightarrow{S21} CO_2(s)$ were combined to:

$$C(s) + 2O(s) \rightarrow CO_2(s) + 2Pt(s). \tag{R7}$$
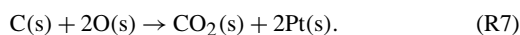
R7 had the same kinetic parameters as S19, and a reaction order of one with respect to O(s). The reduced scheme of Deutschmann valid for purely heterogeneous applications (see Table 3) consisted of 10 reactions R1–R10 and 11 species (4 gaseous and 7 surface) in comparison to the 24 reactions and 20 species (9 gaseous and 11 surface) of the full scheme. The reduced scheme reproduced at all pressures excellently the predicted channel transverse profiles of Fig. 9 and the SPSR catalytic methane conversions of Fig. 10a; the same applied to the SPSR methane conversions under the operating conditions of Fig. 13b that were pertinent to purely catalytic combustion. The differences between the reduced and the full scheme predictions were, for example, less than 1% at any transverse position of Fig. 9 and less than 0.4% in the SPSR catalytic conversions of Figs. 10a and 13b.

Under conditions of appreciable gaseous participation, the reduced catalytic scheme should reproduce the catalytic as well as the gaseous fuel conversion and—although not of particular emphasis in the present investigation—should capture the onset of homogeneous ignition. As discussed in Section 4.1, the OH adsorption/desorption reactions were crucial in describing the inhibiting role of the catalyst during gaseous ignition. It was further stated that CO was produced by the gaseous and consumed mainly by the catalytic pathway and that for the lean conditions of this study removal of the CO adsorption/desorption reactions did not have a strong impact on the already low CO levels and the ensuing CH_4 conversion. The lack of the CO heterogeneous reactions, however, resulted in 10–15% shorter homogeneous ignition distances due to the somewhat higher CO concentrations. Inclusion of the CO adsorption step (as seen in Fig. 12 the CO desorption was less important) could further improve homogeneous ignition predictions:

$$CO + O(s) + Pt(s) \rightarrow CO_2(s) + Pt(s). \qquad (R13)$$
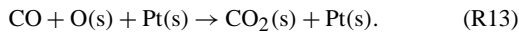
R13 was not an elementary reaction and combined the adsorption and surface oxidation of CO in a single, Eley–Rideal-type reaction. The reaction parameters of R13 were those of S14, the slowest step in the CO surface oxidation chain; therefore, the reaction order with respect to Pt(s) and O(s) was two and zero, respectively. The augmented reduced scheme shown in Table 3 (reactions R1–R13) predicted catalytic and gaseous SPSR methane conversions that were in good agreement with those of the full scheme. In addition, predictions (augmented reduced catalytic scheme/Warnatz) of the CH_4 boundary-layer profiles in the channel-flow reactor at far downstream locations were also in good agreement with those computed with the Deutschmann (full)/Warnatz schemes. The same applied also to homogeneous ignition predictions in the channel-flow reactor; details on the last issue are outside the scope of the present work.

Global catalytic combustion steps similar to those of Eq. (13) (applicable to pure catalytic combustion applications) were also investigated. In the absence of gaseous reactions, the SPSR governing equation [37] becomes

$$(Y_{CH_4,IN} - Y_{CH_4})/\tau = (SV/\rho)\dot{s}_{CH_4} W_{CH_4}, \qquad (14)$$

with τ and SV the reactor residence time and surface-to-volume ratio, respectively. Using Eq. (13) for $\dot{s}_{CH_4}$ and further considering that $[CH_4] = \rho Y_{CH_4}/W_{CH_4}$, Eq. (14) yields for a fixed pressure, SV and τ:

$$\log(Y_{CH_4,IN}/Y_{CH_4} - 1) \propto -E_a/RT. \qquad (15)$$

Computed SPSR plots of $\log(Y_{CH_4,IN}/Y_{CH_4} - 1)$ versus $1/T$ for the scheme of Deutschmann are presented in Fig. 15a for three pressures; the effective
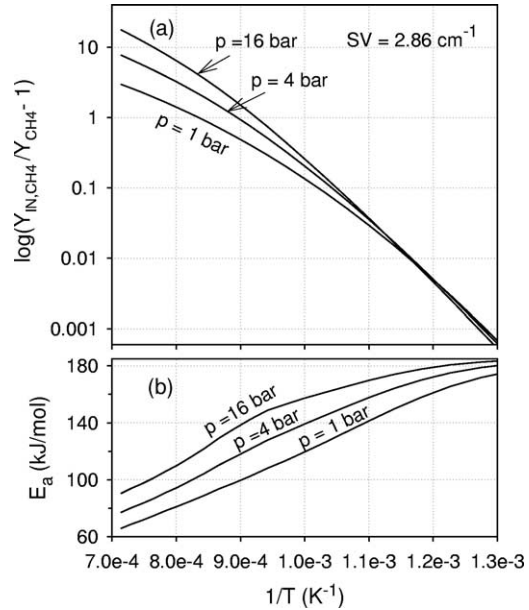
Fig. 15. (a) Plots of $\log(Y_{IN,CH_4}/Y_{CH_4} - 1)$ versus $1/T$ computed in a surface perfectly stirred reactor (SPSR) using the heterogeneous scheme of Deutschmann. The surface-to-volume ratio, the CH_4/air equivalence ratio, and the residence times at each pressure are as in Fig. 10. (b) Effective activation energies calculated from the slope of the plots of Fig. 15a, according to Eq. (15).

activation energies (calculated from the slope of the plots of Fig. 15a) are presented in Fig. 15b. It is clearly seen that in Deutschmann's scheme there exists no constant E_a over the temperature and pressure ranges of interest: E_a varied from 65 to 185 kJ/mol, increasing strongly with decreasing temperature and moderately with increasing pressure. The above discussion has shown that a global step was not consistent with the validated scheme of Deutschmann. Nevertheless, for engineering applications the following global step is proposed, yielding the best fit to the SPSR computations,

$$\dot{s}_{CH_4} = B(p/p_0)^{-n} \exp(-E_a/RT)[CH_4], \qquad (16)$$

with $B = 1.27 \times 10^5$ cm/s, $n = 0.53$, $E_a = 84$ kJ/mol, and $p_0 = 1$ bar. SPSR comparisons between the global step and the full scheme of Deutschmann are provided in Fig. 16 (gaseous chemistry was not included); the agreement in methane conversion is better than $\pm 15\%$ over the extended pressure range 1 bar $\leqslant p \leqslant$ 16 bar.

4.4. High-pressure reactor performance

In recent studies [17] we developed analytical criteria for heterogeneous and homogeneous ignition in 2-D plane channel-flow configurations with uniform
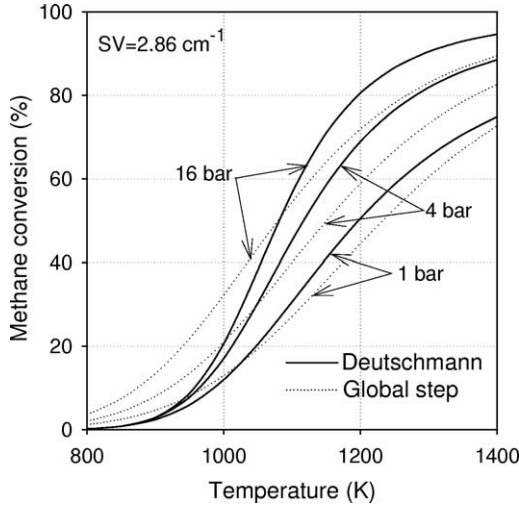
Fig. 16. Computed methane heterogeneous conversions in a surface perfectly stirred reactor (SPSR). Solid lines, scheme of Deutschmann; dotted lines, global step of Eq. (16).

incoming properties and isothermal catalytic walls. The approach was based on a parametric description of the chemically frozen gaseous state for the definition of catalytic ignition and on matched activation energy asymptotics for gaseous ignition. A one-step catalytic reaction (first order with respect to the deficient reactant, as in Eq. (16)) and a one-step large activation energy gaseous reaction were employed. Although the isothermal catalytic wall-boundary conditions were not typical in CST, except possibly in a second-stage catalytic module, the heterogeneous part of the analytical formulation was rich enough to provide, in conjunction with the one-step reaction of Eq. (16), useful insights on high-pressure reactor performance issues such as catalytic fuel conversion and catalytic ignition distance.

The fractional heterogeneous fuel conversion $I_{h,F}(x) = \dot{m}_{h,F}(x)/\dot{m}_{F,\mathrm{IN}}$ was shown to be [17]

$$I_{h,F}(\zeta) = \frac{1}{Le} \int_0^\zeta \frac{1}{\sqrt{2Pr\zeta}} (1/\tilde{Y}_{F,\mathrm{IN}})(\tilde{Y}'_F)_{fr,W}\, d\zeta, \tag{17}$$

where $\dot{m}_{F,\mathrm{IN}} = \rho_{\mathrm{IN}} Y_{F,\mathrm{IN}} U_{\mathrm{IN}} b$ was the incoming fuel mass-flow rate over half the channel domain, $\dot{m}_{h,F}(x)$ the integrated (down to position x) heterogeneous conversion on one catalytic wall, Le the Lewis number of the deficient reactant (fuel), ζ the Graetz number [39] based on the incoming Reynolds number Re,

$$\zeta = x/(bRePr), \quad Re = \frac{\rho_{\mathrm{IN}} U_{\mathrm{IN}} b}{\mu_{\mathrm{IN}}}, \tag{18}$$

and $(1/\tilde{Y}_{F,\mathrm{IN}})(\tilde{Y}'_F)_{fr,W}$ the normalized transverse gradient of the fuel at the wall [17],

$$(1/\tilde{Y}_{F,\mathrm{IN}})(\tilde{Y}'_F)_{fr,W} = \left[(GPDa_s)^{-1} \right.$$
$$\left. + \left[(1/\tilde{Y}_{F,\mathrm{IN}})(\tilde{Y}'_F)_{fr,W} \right]^{-1}_{Da_s \to \infty} \right]^{-1}, \tag{19}$$

with $\tilde{Y}_k = (W_F/\nu_k W k) Y_k$ and ν_k the stoichiometric coefficient of the kth species. In Eq. (19), Da_s was a characteristic surface Damköhler number

$$Da_s = \frac{bBp^{-n} \exp(-E_a/RT_W)}{\alpha_{\mathrm{th,IN}}}, \tag{20}$$

where $\alpha_{\mathrm{th,IN}}$ was the inlet thermal diffusivity and G, P, and $[(1/\tilde{Y}_{F,\mathrm{IN}})(\tilde{Y}'_F)_{fr,W}]_{Da_s \to \infty}$ were monotonically increasing functions of ζ, the last function being the normalized fuel wall gradient at infinitely fast surface chemistry:

$$G = Le\sqrt{2Pr\zeta}\left(\frac{T_W}{T_{\mathrm{IN}}}\right)^{-1},$$
$$P = 1 + 0.158\left(\frac{T_W}{T_{\mathrm{IN}}}\right)^{-1.12} Le^{0.32} Da_s^{0.75} \zeta^{0.13},$$

and

$$\left[(1/\tilde{Y}_{F,\mathrm{IN}})(\tilde{Y}'_F)_{fr,W} \right]_{Da_s \to \infty}$$
$$= (0.43 + 0.45\zeta^{0.35}) Le^{1/3 + 0.19\zeta^{0.35}}$$
$$\times Pr^{1/3 + 0.24\zeta^{0.2}}\left(\frac{T_W}{T_{\mathrm{IN}}}\right)^{0.77\zeta^{0.2}}, \tag{21}$$

with T_W/T_{IN} the wall-to-inlet temperature ratio. Equations (19) and (21) were valid up to $\zeta = 0.16$, which corresponded to a maximum fractional catalytic fuel conversion ($Da_s \to \infty$) of $I_{h,F} \sim 0.43$ for a diffusionally neutral fuel ($Le = 1$). Such maximum fuel conversions were well within the interest of practical CST reactors [1], which usually consist of two catalytic modules with combined fuel conversions of $I_{h,F} \sim 0.5$. Substituting Eqs. (19) and (21) in Eq. (17), the fractional fuel conversion becomes

$$I_{h,F}(\zeta) = \int_0^\zeta \left[F(\zeta, Da_s) + H(\zeta) \right]^{-1} d\zeta, \tag{22}$$

with $F(\zeta, Da_s)$ and $H(\zeta)$ the functions:

$$F(\zeta, Da_s) = (T_W/T_{\mathrm{IN}})/(PDa_s),$$
$$H(\zeta) = Le(2Pr\zeta)^{1/2}$$
$$\Big/ \left[(1/\tilde{Y}_{F,\mathrm{IN}})(\tilde{Y}'_F)_{fr,W} \right]_{Da_s \to \infty}. \tag{23}$$

In the limit of infinitely fast surface chemistry, $F(\zeta, Da_s) = 0$; substituting Eqs. (23) and (21) in Eq. (22), the leading ζ dependence of the fractional fuel conversion is shown to be $I_{h,F}(\zeta) \propto \zeta^{0.85}$. Since
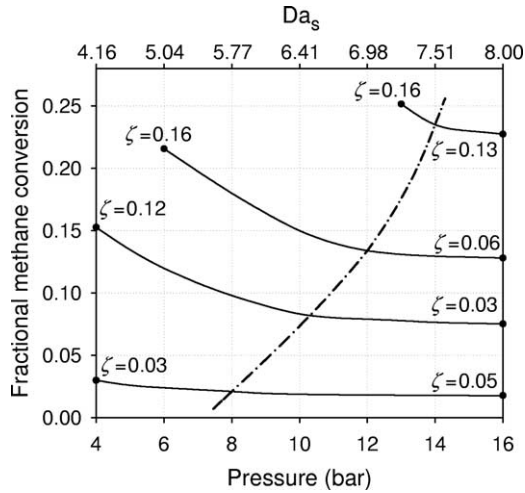
Fig. 17. Fractional methane catalytic conversion as a function of pressure, computed from Eq. (17) using the global step of Eq. (16). Four different cases are plotted (solid curves), characterized by different ranges of the nondimensional parameter ζ. The top horizontal axis provides the surface Damköhler numbers Da_s. The area to the right of the dashed-dotted line delineates the regimes over which the fractional catalytic fuel conversion is, in each case, constant within 5%.

ζ is inversely proportional to pressure (see Eqs. (18)), a pressure increase in a catalytic channel of a fixed geometry and inlet velocity would always result in a decrease of the fractional fuel conversion, which is a direct consequence of the higher reactor mass throughput. However, this was not necessarily the case under finite-rate surface chemistry conditions. Since $Da_s \propto p^{1-n}$ (considering the p^{-1} dependence of the thermal diffusivity in Eq. (20)), for all $n < 1$ the function $F(\zeta, Da_s)$ decreased with increasing pressure and, therefore, the integrand of Eq. (22) increased with increasing pressure; in conjunction with the drop of ζ with increasing pressure, the integral of Eq. (22) could become (under a proper combination of geometric and surface reaction parameters) independent of pressure over an extended pressure range. For a system away from the mass-transport limit, this simply implied that the increased reactor mass throughput was counterbalanced by the enhanced reactivity that led to the increased catalytic fuel conversion at higher pressures. The attainment of pressure-independent fractional fuel conversion was highly desirable in many practical systems, for example, gas turbines, as it resulted in a constant temperature rise across the catalytic reactor during pressure ramps and load changes. The above reasoning could also explain the nearly pressure-independent temperature rise reported recently [40] in a subscale gas

turbine honeycomb-type catalytic reactor (Pd-based), operated at 5 bar $\leqslant p \leqslant$ 15 bar.

Calculated fractional fuel conversions from Eq. (22) are illustrated in Fig. 17, for $n = 0.53$, 4 bar $\leqslant p \leqslant$ 16 bar, $T_W/T_{IN} = 2$ and typical for fuel-lean CH_4/air mixtures $Le = 0.95$ and $Pr = 0.7$. Four cases are presented, each characterized by a different range of nondimensional distances ζ and the same Da_s for a given pressure: $Da_s = 8$ at $p = 16$ bar, while at different pressures Da_s scaled according to Eq. (20). Depending on the surface reactivity and on the channel geometrical parameters, a nearly constant fractional fuel conversion could be attained over a specific pressure range for each case. The higher the fractional fuel conversion of each case, the narrower the pressure range over which a constant value of $I_{h,F}$ could be maintained. Since in practical systems the surface temperature is directly linked to the catalytic reactivity, an even broader pressure range of constant $I_{h,F}$ could be achieved compared to the range predicted by the analysis of Eq. (22), which considered the surface temperature decoupled from the kinetics.

The light-off distance (catalytic ignition distance) is also of prime interest in practical systems and its minimization is a major reactor design goal. Within the context of isothermal channel catalytic walls, a catalytic ignition criterion was presented [17],

$$Da_{s,ig} = (T_W/T_{IN})^{3/2}Le^{-2/3}\zeta^{-1/2}. \qquad (24)$$

The ignition criterion of Eq. (24) was a good approximation to the rigorous criterion presented also in [17] and provided the nondimensional light-off distance (ζ) required to achieve a fuel conversion ~50% of the maximum attainable (mass-transport limited, $Da_s \to \infty$) conversion. For $n = 0.5$, the physical light-off distance was independent of pressure (see Eqs. (24), (20), and (18)); it could be further reduced with increasing pressure if $n < 0.5$. The reason for this behavior was that, even though in the developing section of a channel the local transverse transport rates increased with increasing Reynolds number (and hence with pressure), the surface reactions could still cope with this augmentation provided that the catalytic reactivity increased at an appropriate pressure-dependent rate.

5. Conclusions

The catalytic reactivity of fuel-lean methane/air mixtures over Pt was assessed with in situ Raman measurements of major species and temperature in a channel-flow catalytic reactor operated at pressures and temperatures in the ranges 4 bar $\leqslant p \leqslant$ 16 bar and 780 K $\leqslant T \leqslant$ 1250 K, respectively. The experiments were compared with 2-D numerical predictions

that included elementary hetero/homogeneous reaction schemes and detailed transport. The following are the key conclusions of this study.

1. The measured catalytic reactivity increased with increasing pressure over the entire range 4 bar $\leqslant p \leqslant$ 16 bar. Predictions with two heterogeneous reaction schemes, those of Deutschmann and Vlachos, have shown that both schemes captured the increase in catalytic reactivity with increasing pressure. However, only the former scheme yielded a quantitative agreement with the measurements over the aforesaid pressure range.

2. Crucial for the correct prediction of the measured catalytic reactivity was the ability of the heterogeneous reaction schemes to capture the reduction in surface free-site coverage (and the corresponding increase in oxygen coverage) with increasing pressure. This effect restrained the rate of increase of the catalytic reactivity with increasing pressure.

3. The gas-phase pathway could not be ignored at high pressures. Even in the absence of homogeneous ignition, the gaseous preignition chemistry could contribute significantly to the fuel conversion at high pressures. The regimes of reactor residence time and surface-to-volume ratio (SV), over which the impact of the gaseous reaction pathway was important, were delineated with computations in a surface perfectly stirred reactor. It was shown that the numerical simulations of practical high-pressure catalytic combustion systems should consider the gaseous chemistry, notwithstanding the typically large SV of these systems.

4. Using the heterogeneous scheme of Deutschmann, a reduced catalytic reaction scheme was derived, valid for purely heterogeneous combustion. The scheme was capable of predicting accurately the catalytic methane conversion in the absence of gaseous chemistry. A second, augmented reduced catalytic scheme for combined hetero/homogeneous combustion was also derived, which was capable of reproducing the catalytic and gaseous fuel conversions as well as the onset of homogeneous ignition.

5. A global catalytic step could not reproduce the measured catalytic reactivity over the entire pressure range 4 bar $\leqslant p \leqslant$ 16 bar. However, a best-fit global step has been derived for engineering applications, yielding catalytic methane conversions in an SPSR within $\pm 15\%$ of those computed with the validated scheme of Deutschmann, over the extended pressure range 1 bar $\leqslant p \leqslant$ 16 bar.

6. It was shown that, under a certain combination of catalytic reactivity and geometrical reactor parameters, the fractional methane catalytic conversion (and, hence, the temperature rise across a channel-flow reactor) could become independent of pressure, when all other operating parameters (inlet velocity and inlet temperature) were fixed. This property was highly desirable during pressure ramps and load changes in many practical systems, such as gas-turbine catalytic reactors.

Acknowledgments

References

[1] R. Carroni, V. Schmidt, T. Griffin, Catal. Today 75 (2002) 287–295.

[2] A. Schlegel, P. Benz, T. Griffin, W. Weisenstein, H. Bockhorn, Combust. Flame 105 (1996) 332–340.

[3] M. Reinke, J. Mantzaras, R. Schaeren, R. Bombach, W. Kreutner, A. Inauen, Homogeneous Ignition in High-Pressure Combustion of Methane/Air over Platinum: Comparison of Measurements and Detailed Numerical Predictions, Proc. Combust. Inst. 29 (2002) 1021.

[4] C. Appel, J. Mantzaras, R. Schaeren, R. Bombach, A. Inauen, B. Kaeppeli, B. Hemmerling, A. Stampanoni, Combust. Flame 128 (2002) 340–368.

[5] O. Deutschmann, L.I. Maier, U. Riedel, A.H. Stroemman, R.W. Dibble, Catal. Today 59 (2000) 141–150.

[6] A.B. Mhadeshwar, P. Aghalayam, V. Papavassiliou, D.G. Vlachos, Surface Reaction Mechanism Development for Platinum Catalyzed Oxidation of Methane, Proc. Combust. Inst. 29 (2002) 997.

[7] P. Aghalayam, Y.K. Park, N. Fernandes, V. Papavassiliou, A.B. Mhadeshwar, D.G. Vlachos, J. Catal. 213 (2003) 23–38.

[8] D.A. Hickman, L.D. Schmidt, AIChE 39 (1993) 1164–1177.

[9] O. Deutschmann, L.D. Schmidt, AIChE 44 (1998) 2465–2477.

[10] H. Haerle, A. Lehnert, U. Metka, H.R. Volpp, L. Willms, J. Wolfrum, Chem. Phys. Lett. 293 (1998) 26–32.

[11] P. Ciambelli, V. Palma, S.F. Tikhov, V.A. Sadykov, L.A. Isupova, L. Lisi, Catal. Today 47 (1999) 199–207.

[12] G. Groppi, W. Ibashi, E. Tronconi, P. Forzatti, Chem. Eng. J. 82 (2001) 57–71.

[13] O. Deutschmann, R. Schmidt, F. Behrendt, J. Warnatz, Numerical Modeling of Catalytic Ignition, Proc. Combust. Inst. 26 (1996) 1747.

[14] Y.K. Park, P. Aghalayam, D.G. Vlachos, J. Phys. Chem. A 103 (1999) 8101–8107.

[15] R.W. Sidwell, H. Zhu, R.J. Kee, D.T. Wickham, C. Schell, G.S. Jackson, Catalytic Combustion of Premixed Methane-Air on a Palladium-Substituted Hexaluminate Stagnation Surface, Proc. Combust. Inst. 29 (2002) 1013.

[16] J. Mantzaras, P. Benz, Combust. Flame 119 (1999) 455–472.

[17] J. Mantzaras, C. Appel, Combust. Flame 130 (2002) 336–351.

[18] C. Appel, J. Mantzaras, R. Schaeren, R. Bombach, B. Kaeppeli, A. Inauen, An Experimental and Numerical Investigation of Turbulent Catalytically Stabilized Channel Flow Combustion of Hydrogen/Air Mixtures over Platinum, Proc. Combust. Inst. 29 (2002) 1031.

[19] A. Brockhinke, P. Andresen, K. Kohse-Höinghaus, Appl. Phys. B 61 (1995) 533–545.

[20] B. Steiner, Ph.D. thesis, The University of Stuttgart (2002).

[21] S. Eisenberg, Diploma thesis, Max-Planck-Institut für Strömungsforschung, Göttingen (1995).

[22] U. Dogwiler, J. Mantzaras, P. Benz, B. Kaeppeli, R. Bombach, A. Arnold, Homogeneous Ignition of Methane/Air Mixtures over Platinum: Comparison of Measurements and Detailed Numerical Predictions, Proc. Combust. Inst. 27 (1998) 2275.

[23] R.J. Kee, G. Dixon-Lewis, J. Warnatz, M.E. Coltrin, J.A. Miller, A Fortran Computer Code Package for the Evaluation of Gas-Phase Multicomponent Transport Properties, Report No. SAND86-8246, Sandia National Laboratories, 1996.

[24] S. Patankar, Numerical Heat Transfer and Fluid Flow, Hemisphere, New York, 1980, p. 131.

[25] U. Dogwiler, P. Benz, J. Mantzaras, Combust. Flame 116 (1999) 243–258.

[26] J. Mantzaras, C. Appel, P. Benz, Catalytic Combustion of Methane/Air Mixtures over Platinum: Homogeneous Ignition Distances in Channel Flow Configurations, Proc. Combust. Inst. 28 (2000) 1349.

[27] L.L. Raja, R.J. Kee, O. Deutschmann, J. Warnatz, L.D. Schmidt, Catal. Today 59 (2000) 47–60.

[28] V.D. Vlachos, personal communication.

[29] J. Warnatz, M.D. Allendorf, R.J. Kee, M.E. Coltrin, Combust. Flame 96 (1994) 393–406.

[30] J. Warnatz, U. Maas, Technische Verbrennung, Springer-Verlag, New York, 1993, p. 101.

[31] GRI-3.0, Gas Research Institute, http://www.me.berkeley.edu/gri_mech, 1999.

[32] J. Warnatz, R.W. Dibble, U. Maas, Combustion, Physical and Chemical Fundamentals, Modeling and Simulation, Springer-Verlag, New York, 1996, p. 69.

[33] R.J. Kee, F.M. Rupley, J.A. Miller, The Chemkin Thermodynamic Data Base, Report No. SAND87-8215B, Sandia National Laboratories, 1996.

[34] R.J. Kee, F.M. Rupley, J.A. Miller, Chemkin II: A Fortran Chemical Kinetics Package for the Analysis of Gas-Phase Chemical Kinetics, Report No. SAND89-8009B, Sandia National Laboratories, 1996.

[35] M.E. Coltrin, R.J. Kee, F.M. Rupley, Surface Chemkin: A Fortran Package for Analyzing Heterogeneous Chemical Kinetics at the Solid Surface-Gas Phase Interface, Report No. SAND90-8003C, Sandia National Laboratories, 1996.

[36] I. Glassman, Combustion, third ed., Academic Press, London, 1996, p. 156.

[37] H.K. Moffat, P. Glarborg, R.J. Kee, J.F. Grcar, J.A. Miller, Surface PSR: A Fortran for Modeling Well-Stirred Reactors with Gas and Surface Reactions, Report No. SAND91-8001, Sandia National Laboratories, 1993.

[38] G.C. Snow, W.V. Krill, E.K. Chu, R.K. Kendall, Mechanisms and Kinetics in Catalytic Combustion, Report No. EPA-600/9-84-002, 1984, p. 105.

[39] W.M. Kays, Crawford, Convective Heat and Mass Transfer, third ed., McGraw–Hill, New York, 1993, p. 128.

[40] R. Carroni, T. Griffin, J. Mantzaras, M. Reinke, Catal. Today 83 (2003) 157–170.